Synthesis, Characterization and Applications of Multi-component and Multi-functional Composites with Nanostructured Conducting Polymers

by

Selcuk Poyraz

A dissertation submitted to the Graduate Faculty of
Auburn University
in partial fulfillment of the
requirements for the Degree of
Doctor of Philosophy

Auburn, Alabama
August 2, 2014

Keywords: nanostructured conducting polymers, composites

Approved by

Xinyu Zhang, Chair, Associate Professor of Polymer and Fiber Engineering
Maria Lujan Auad, Associate Professor of Polymer and Fiber Engineering
Gisela Buschle-Diller, Professor of Polymer and Fiber Engineering
Sabit Adanur, Professor of Polymer and Fiber Engineering

Abstract

Multi-component and multi-functional nanostructured conducting polymer (CP) based composites were prepared through different methods to obtain materials with academic and industrial interest gathering properties.

In two different studies; facile, simple and one-step seeding template-assisted oxidative polymerization reactions of CPs were conducted to synthesize nanocomposites made up of poly(ortho-toluidine) (POT) and polyaniline (PANI) nanofibers (NFs) decorated with different metal (Au/Cu, Ag) nanoparticles (NPs). Enhanced bio-sensing property for glucose and excellent antibacterial activity against both Gram-positive and Gram-negative bacteria strains were meant to be exhibited by these nanocomposites, respectively. As the reaction media, three different metal salts' aqueous solutions were used. Gold (I) chloride (AuCl), copper (II) chloride ($CuCl_2$) and silver nitrate ($AgNO_3$) salts were, individually, dissolved in DI water to prepare their solutions used in two different studies. They eliminated the extra use of harsh chemicals like hydrochloric acid (HCl), oxidative agents like ammonium peroxydisulfate (APS, $(NH_4)_2S_2O_8$) and also large amounts of in/soluble templates like zeolites, opals and surfactants by acting both as the dopant and oxidant for POT and PANI. Vanadium pentoxide (V_2O_5) sol-gel NFs were assisting these reactions not only as well-known seeding agents to ensure the NF morphology formation for the resulting CPs, but also as the auxiliary oxidative agents to enhance the overall oxidative potential of the reaction solutions.

In the third study, nanostructured CPs, e.g. polypyrrole (PPy) NPs, were used as the microwave absorbing coating on the surface of devulcanized ground tire rubber (dGTR) particles to grow carbon nanotubes (CNTs) on their surface via previously studied "PopTube" approach. Throughout this study; (i) GTR waste was initially devulcanized by short-term microwave irradiation in 4 min., and the virgin rubber ingredient inside them was effectively collected by extraction to be used for the manufacturing of new rubber products, (ii) and then value-added, CNT decorated dGTR particles were also produced as the promising reinforcing agents to make advanced polymeric composite structures.

The goal of all these studies was to build a substantial background for different industrial applications, i.e. non-enzymatic/amperometric glucose sensors, excellent antibacterial agents and promising reinforcing agents for polymeric composites, by utilizing the knowledge gained from the chemical synthesis reactions and the instrumental characterizations. In order to investigate, control, improve and characterize numerous properties of CP-based nanocomposites and to determine the effects of different reaction parameters on the final product morphology and properties, the above mentioned projects were undertaken in details throughout this dissertation.

Acknowledgments

The author would like to express his thanks to his advisor and mentor, Dr. Xinyu Zhang, for his time, guidance, and judicious advice. The author also expresses his gratitude to all his committee members and university reader for their precious suggestions.

The author is owed special thanks to all his research group partners for their collaboration and help. Appreciation is also owed to the Department of Polymer and Fiber Engineering for the welcoming study and working environment. The author also expresses his gratitude to all his friends in Polymer and Fiber Engineering Department and in Auburn, for providing him ongoing support throughout these five years. The author would like to thank the Turkish Ministry of Education for the financial aid in sponsoring him during his graduate studies.

The author finally would like to express his most sincere thanks to his parents, Kemalettin and Alime, and his older sister, Seval, for their sincere love and support. The author's appreciation from the bottom of his heart also goes to his wife, Tuba, for her ongoing love, support and encouragement. Finally, the author would like to express his infinite appreciation to the almighty creator for bestowing him all the skills and ability to think.

Table of Contents

List of Tables

List of Figures

CHAPTER 1

One-step Synthesis and Characterization of Poly (ortho-toluidine) Nanofiber/Metal Nanoparticle Composite Networks as Non-enzymatic Biosensors

1.1 Introduction

Since their famous introduction to the scientific society around 40 years ago,[1] conducting polymers (CPs) have gone through unexpectedly rapid and continuous advancements.[2] Due to their uniquely combined mechanical/electronic properties from conventional polymers/metals, in one structure, these materials were commonly called as "synthetic metals[2]" and have been of particular interest for many researchers from both academia and industry.[3,4] Throughout the time, CPs have been carefully observed, and witnessed to participate in revolutionary developments which boosted their utilization for the applications of organic light-weight battery electrodes, electrochromic displays, electromagnetic shielding devices, drug delivery, anti-corrosion coatings, catalysis, sensory and so on (Figure 1).[5-9]

Compared to all other CPs, polyaniline (PANI) has attracted much more attention[3] with respect to its superior properties such as low cost and high polymerization yield,[10] tunable electrical conductivity,[11] long-term environmental stability,[12] various oxidation states[13] and reversible (acid/base) doping/dedoping characteristics associated with its structural chain nitrogen.[14]

Figure 1. Different applications of CPs in; a) an electrochromic display, b) an electromagnetic shielding component, c) a glucose sensor

On the other hand, the negative features of PANI, e.g. poor solubility in common organic solvents, infusible polymeric backbone, poor thermal stability and strong hydrogen bonding interactions between the amine groups at its adjacent chains, which originate from the very common way of PANI's chemical oxidative polymerization in acidic medium, have been restricting its practical uses in aforementioned applications.[12-15]

In order to overcome these issues and to gain deeper insight into PANI, multiple strategies have been pursued.[16] Among all, one of the commonly applied methods is using a methyl (-CH_3) group blockage[3] at the ortho position of the aniline's aromatic ring to obtain a processable PANI derivative called poly (ortho-toluidine) (POT)[16] (Figure 2). Although, the electrical conductivity of POT is relatively lower than that of PANI[5] (the increase in torsion between adjacent rings causes a decrease in the extent of conjugation on the polymeric chain upon the introduction of -CH_3 groups)[3] yet it has been extensively investigated in diverse studies as an active ingredient. For instance; Wan *et al.* investigated different properties of POT as an alternative to PANI,[3] Reddy *et al.* used POT for the direct synthesis of composite nanostructures with gold (Au), silver (Ag) and platinum (Pt) NPs,[5,14] Han *et al.* derived POT nanotubes from its

nanofibers (NFs) for the controlled drug release application and also synthesized core/shell composites of POT with Au,[7,11] Blaz *et al.* utilized POT to support cobalt (Co(II)) for the oxidation of alkenes[8] and Choudhury *et al.*, Ding *et al.* and Bavastrello *et al.* synthesized POT composites with multi-wall carbon nanotubes (MWCNTs) to improve its electrical conductivity and other related properties.[12,15,16] Moreover, its advantageous properties over PANI, e.g. faster switching times between its reduced/oxidized states,[12,14-16] better solubility,[17] long-term stability[14] and interesting electro-optical properties,[5] facilitate the characterization and easier processing of POT[4,17] for its use in common technological applications of field effect transistors, light-emitting diodes, solar cells, immunodiagnostic assay, smart windows and biosensors.

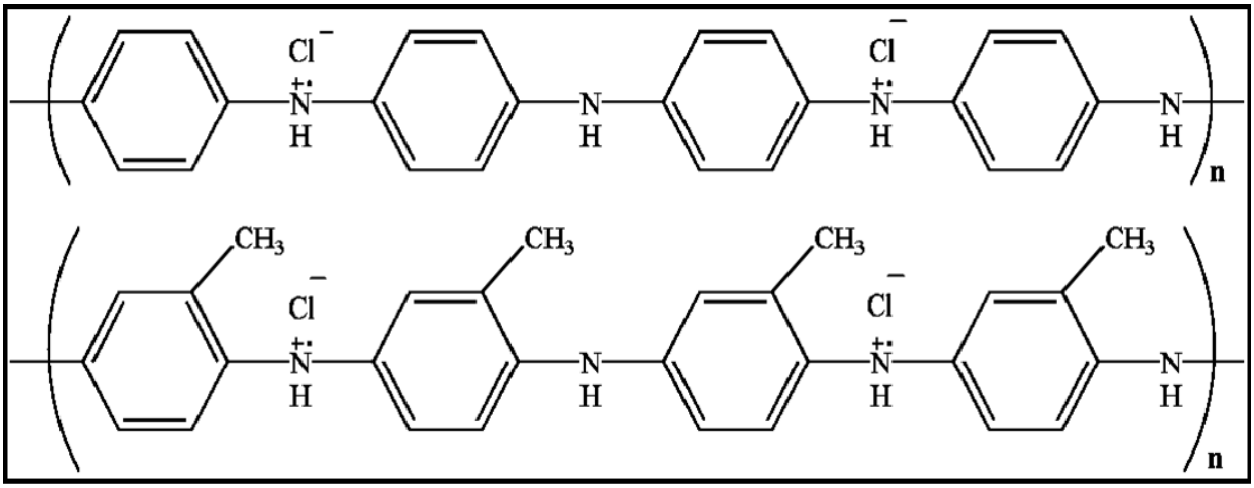

Figure 2. Chemical structures of PANI (top) and POT (bottom) in their emeraldine salt (conducting) forms

As a result of the continuous studies in nanoscale science and technology, especially during the past few years, significance of the synthesis and utilization of nanostructured CPs at different morphologies/dimensions[13,18-20] have been very well understood. The reason is simple

that the nanoscale CPs possess and exhibit interestingly different physico-chemical properties, e.g. larger specific surface area and lower effective density[5,21] from those shown by their bulk versions which promote their utilization to construct functionally sophisticated systems.

In this respect, intensive research efforts have been spent on the studies investigating the different precise control, manipulation and synthesis method development techniques[10] to generate nano-sized hybrid composite systems of CPs with different engineering materials such as carbon nanotubes (CNTs) and metal particles/fibers. Among all, the special emphasis has been given to the composites of cleverly combined CP NFs[6] with different metal nanoparticles (NPs).[11] This is simply because of the easier preparation, long-term mechanical stability, excellent electronic features (high capacitance and charge transfer properties) and benign nature of CP NFs that expedites the immobilization of metallic NPs within their 1-D morphology. Considering the fact about their synergistic and complementary behavior to each other,[9,12] these nanocomposites have been proven to exhibit superior performances over those of their sole components in terms of a host/guest relationship, without any compromise.[22-25]

So far, various attempts have been made, including the in-situ,[4-6] ex-situ[21] and electrochemical synthesis[26] methods to achieve such nanocomposite matrices with versatile multifunctionality and desired properties. Here, the major advantage of the in-situ protocol[17,22] lies in its possibility of "simultaneous CP NF/metal NP formation" which assures the substantial binding of compounds to each other via either strong electrostatic forces or hydrogen bonding.[12] Meanwhile, this principle remains as the challenging part of this method, since the size and morphology control of the resulting nanocomposite must be handled properly during the synthesis reaction.[5]

To exploit the full potential of the above mentioned nanocomposites, they have been used in sensory applications for the detection of biomolecules in physiological fluids, i.e. as glucose sensors. In this field, although the glucose oxidase (GOx)-based sensors have been respected with their high sensitivity and selectivity for glucose, several major disadvantages of these sensors are restricting their applications; such as their intrinsically poor long-term stability,[27] high cost of enzymes,[28] critical operation conditions[28] and complicated immobilization process requirements.[29] Furthermore, the catalytic performance of GOx usually gets deteriorated from the environmental conditions, i.e. temperature, pH level, humidity, toxic chemicals, ionic detergents and so on.[28] Thus, the inclination for GOx-based sensors has been shifted and researchers started spending their efforts to obtain different types of (CP, CNT or metal NP based) non-enzymatic, amperometric biosensors with excellent long-term stability, high sensitivity, reproducibility, selectivity and fast response times as superior alternatives to their GOx-based versions.[30-35] In this context, Zhang *et al.* synthesized nickel (Ni)/multi-walled CNT composites,[27] Luo *et al.* developed the Cu NP modified graphene sheets,[28] Huang *et al.* prepared the electrochemically grown Cu nanobelt electrodes,[29] Kang *et al.* electrochemically deposited Cu nanoclusters on Nafion-solubilized multi-walled CNT films,[36] Yan *et al.* assembled the Au NPs on the surface of silver chloride@PANI core-shell nanocomposites,[37] Feng *et al.* constructed the Au NP-chitosan composite films,[38] Bai *et al.* developed the 3-D Au film electrodes[39] and recently our group synthesized the intercalated Pt@PPy NF composites[40] as promising non-enzymatic glucose sensor materials.

Indeed, glucose sensors are one of the most abundant biosensors that have been continuously developed and commonly used for the areas of clinical diagnostics, health care, biomedical science and food industry during the last 50 years.[30] More importantly, since the

precise measurement and tracking of glucose level in blood is a crucial clinical test for both the early diagnosis and tracking of diabetes mellitus (a group of metabolic diseases from which more than 350 million people world wide are suffering) and to avoid its related emergencies such as hypoglycemia or hyperglycemia,[27] many researchers have devoted their studies to obtain materials with salient properties for this application. As a result, a very large demand and market share have been generated for the non-enzymatic glucose sensors and relevant materials.[31]

Thus, in order to both properly address this demand/market share and to eliminate any kinds of structural or economical shortages of non-enzymatic glucose sensors that have been prepared so far, in this study, Au and Cu NP embedded POT NF networks (POT-Au/Cu) were synthesized. Through a facile and efficient "vanadium pentoxide (V_2O_5) NF-seeded oxidative polymerization reaction" and a "redox/complexation process" that took place between o-toluidine monomers and corresponding metal cations in aqueous medium at ambient temperature, POT-Au/Cu nanocomposites were obtained in one-step and an environmentally friendly manner.[23,25,40] During these reactions, o-toluidine monomers were oxidized to form POT NFs while the Au^{+} or Cu^{2+} cations were reduced to form their NPs which would be readily immobilized within POT matrix and eventually would yield the hybrid CP NF/metal NP composite networks. Therefore, both the simultaneous formation of such nanocomposites would be guaranteed and significance of the well-known "V_2O_5 NF-seeded polymerization technique" would be once more emphasized via this study. Furthermore, the as-synthesized nanocomposites are speculated to exhibit excellent charge transfer, electrocatalysis and sensory properties as a result of the enhanced interfacial interactions between their CP and metallic counterparts.[5] So, they are expected to be the materials of preference to fabricate high performance catalysts and/or non-enzymatic, amperometric biosensors for glucose.

1.2 Experimental section

1.2.1 Materials and methods

The materials used in this study include; o-toluidine (99%, Alfa Aesar), gold chloride (AuCl, 99.9%, Alfa Aesar), copper (II) chloride ($CuCl_2$, 98% anhydrous, Alfa Aesar), ammonium peroxydisulfate ($(NH_4)_2S_2O_8$, APS, 98%, Alfa Aesar), colloidal graphite paste (isopropanol base, Electron Microscopy Sciences), D-glucose (anhydrous, J.T. Baker), uric acid (UA, 99%, Alfa Aesar), 4-acetamidophenol (AP, 98%, Sigma-Aldrich), ascorbic acid (AA, UPS grade, AMRESCO) and acetone (J.T. Baker). The V_2O_5 sol-gel NF was prepared based on previously reported method (Bailey, J. K.; Pozarnsky, G. A.; Mecartney, M. L. *J. Mater. Res.* 1992, 7, 2530) by using ammonium metavanadate (NH_4VO_3, 99.5%, Acros Organics) and Dowex Marathon (H) ion exchange resin (Sigma Aldrich).

1.2.2 One-step synthesis of POT-Au/Cu nanocomposites

In a typical experiment, 1 mL of V_2O_5 sol-gel NF was gently introduced into 50 mL pre-stabilized DI water under magnetic stirring and changed its color to orange. After 10 min. magnetic stirring at ambient conditions, 0.1 mL of o-toluidine monomer was added into this medium. Upon the preliminary oxidative interactions between monomers and V_2O_5, starting from the third minute of the following 10 min. stirring, the well-dispersed fibrous structures were being formed while changing the medium color to greenish yellow. Eventually, in order to obtain the stock 0.02 M concentrated solutions of different metal salts, required amounts of AuCl and $CuCl_2$ was weighed and added into each system.

It is noteworthy that, due to the oxidative potential difference between these two metal salts, the color of the reaction solution was either turned into turquoise as in $CuCl_2$ system or was spontaneously darkened as in AuCl system, which typically happens during the oxidative

polymerization of CPs, indicating the formation/dispersion of fibrous POT precipitates. Thus, in order to compensate this oxidative potential difference, catalytic amount (0.057 g) of APS was finally added in $CuCl_2$ system after 10 min. extra stirring and this caused the expected darkening in reaction medium color as in AuCl system.

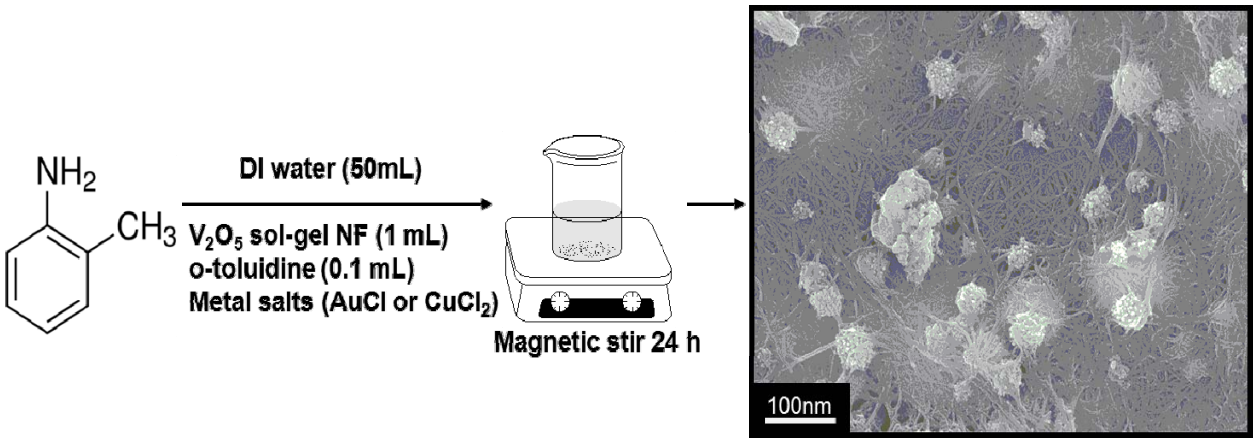

Figure 3. Schematic representation of the one-step synthesis of POT-Au/Cu nanocomposites

A further reaction time period of 24 h was given to both systems in order to obtain POT NFs decorated with corresponding metal NPs. At the end, the resulting precipitates were suction filtered while getting washed with copious amounts of DI water and acetone, respectively. The damp precipitates were allowed to dry overnight in an oven at 80 °C. The yield of nanocomposite powders was ~10 mg and ~20 mg, respectively.

1.2.3 Structural characterization of the as-obtained POT-Au/Cu nanocomposites

Scanning electron microscopy (SEM) and energy dispersive X-ray (EDX) characterization of the nanocomposite networks were performed on a JEOL JSM-7000F instrument. High resolution transmission electron microscopy (HR-TEM) and selected area electron diffraction (SAED) characterizations were performed on a JEOL 2100F TEM

instrument operated at 200 kV. UV-Visible light absorbance spectra of the nanocomposite networks were obtained from a SHIMADZU UV-2450 spectrophotometer. Fourier Transform Infrared (FTIR) analysis was conducted by a Thermo Nicolet 6700 FTIR instrument. Thermal gravimetric analysis (TGA) of the nanocomposite networks were performed on a TA Q2000 system. X-Ray diffractometry (XRD) analysis of the nanocomposite samples were performed on a Rigaku powder X-Ray diffractometer.

1.2.4 Electrochemical characterization of the as-obtained POT-Au/Cu nanocomposites

The electrochemical tests of the nanocomposite networks were performed on a CHI-601D workstation that was equipped with a conventional three-electrode cell system. First, to take the open circuit potential (OCP) measurements, the conventional three-electrode cell system was immersed into the reaction media (Figure 4). Here, platinum (Pt) gauze was used as the working electrode (WE) while a Pt wire was used as the counter (CE) and Ag/AgCl as the reference (RE). Before taking the measurements and adding reactants, 0.01 M of potassium nitrate (KNO_3) was added into 50 mL DI water medium, under magnetic stirring, in order to decay and stabilize the reaction potential at a steady state that took at most 20 min. The open circuit condition was applied to the electrode cell system while no current was passing through and the potential difference between the WE and RE was monitored continuously. A standard synthesis process (above mentioned) was performed and the overall change in its potential was monitored simultaneously as a function of time.

Next, the WE was prepared for the following cyclic voltammetry (CV) and amperometric glucose sensing applications via casting 0.5 mg of the POT-Au/Cu onto a polished graphite electrode through the colloidal graphite paste and getting dried for 15 min. at room temperature prior to its use. Again, Pt wire was used as the CE and Ag/AgCl was used as the RE for these

applications. The cyclic voltammetry (CV) was either performed in 0.1 M aq. sodium hydroxide (NaOH) solution within the cyclic potential range of -0.8 V to 0.6 V at 20 mV/s scan rate or in 0.1 M aq. sulphuric acid (H_2SO_4) solution within the cyclic potential range of -0.2 V to 1.2 V at 10 mV/s scan rate. Without and with the presence of glucose at various concentrations (0-10 mM), 0.1 M aq. NaOH was used for the glucose sensing applications and corresponding electrode responses were recorded simultaneously. The amperometric test was performed at an applied potential of 0.1 V in the same solution, into which 1 mM glucose was successively injected (up to 30 mM) at an interval of 60 s, under constant magnetic stirring. The electrode response was taken as the difference between the steady-state and background current.

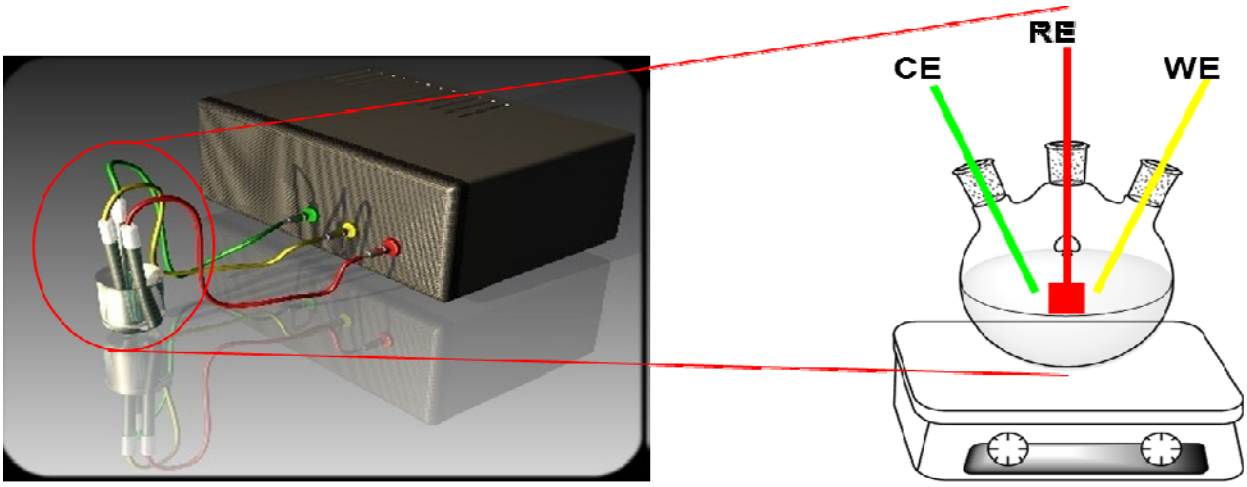

Figure 4. Schematic representation of the workstation used for the electrochemical experiments

The overall electrode selectivity for glucose was determined by using the same testing system with the presence of different interfering agents such as uric acid (UA), ascorbic acid (AA) and 4-acetamidophenol (AP), at their physiological levels. The experiment was conducted

in 0.1 M aq. NaOH solution, at 0.3 V cell voltage, and with successive additions of 5 mM glucose, 0.02 mM UA, 0.1 mM AP and 0.1 mM AA at 60s intervals, respectively.

1.3 Results and discussion

1.3.1 OCP measurement results of the one-step nanocomposite synthesis reactions

The results obtained from the in-situ monitoring of the nanocomposite network synthesis reactions are shown in Figure 5. The results clearly revealed the changes occurred in the oxidation potentials of two different systems. Here, not only the critical seeding agent role that V_2O_5 NFs played in our group's previous studies, but also their well-known oxidative potential enhancer role in different metal salts' aqueous solutions could be clearly observed.

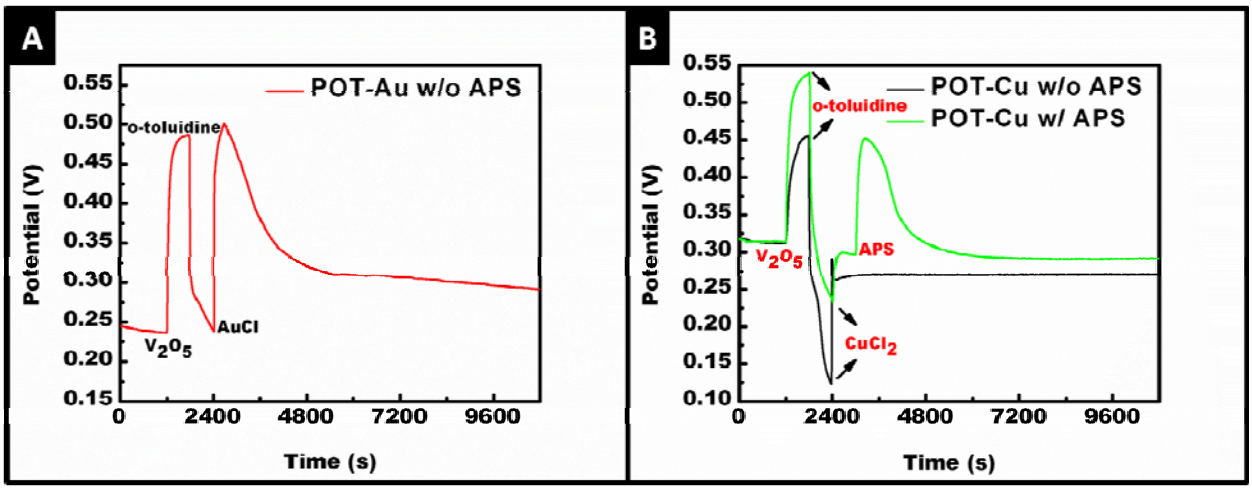

Figure 5. OCP results obtained from the; (A) POT-Au and (B) POT-Cu nanocomposite networks' in-situ monitored synthesis reactions

Since, just the oxidative potentials of metal salt solutions were impotent to initiate the polymerization reactions in an acceptable time manner, the addition of catalytic amount of V_2O_5

NFs in the reaction media had; (i) enhanced the overall oxidative potential of both solution systems beyond 0.45 V, (ii) helped metal salts, via partially pre-oxidizing the monomers, to pass the oxidation threshold to expedite the oxidation of o-toluidine, and (iii) significantly accelerated the polymerization reactions (within 3h reached the steady-state). Meanwhile, the as-synthesized POT exhibited homogeneous NF morphology, due to the seeding effect of V_2O_5 NFs.

1.3.2 Structural characterization results of the POT-Au/Cu nanocomposites

The SEM images of POT-Au/Cu nanocomposite networks are shown in Figure 6. Homogenously embedded or protruding Au NP clusters with ~275 nm average diameters can be seen on the images (Figure 6A and C). Highly dense and straight POT NF network with a narrow pore distribution can be observed from the POT-Au nanocomposite structure (Figure 6B). The bright, prominent spots with ~500 nm average diameters can be seen in Figure 6C, indicating the Au NP clusters with high electron densities embedded inside the POT NF matrix (Figure 7A). The EDX analysis of these spots indicates that they are composed of elemental Au (Table 1). The POT NF network, composed of ~35 nm average diameter fibers, has very tight nanopores formed among the NFs interspaces (Figure 6B and C). On the other hand, homogenously distributed and POT NF covered Cu NP clusters with average diameters of ~475 nm can be seen on the POT-Cu nanocomposite images (Figure 6D and F). Most probably due to the oxidative potential difference between these two systems, which was mentioned during the nanocomposite synthesis in the experimental section, the fibers obtained within the POT-Cu nanocomposite have larger diameters (~40 nm) and are apparently shorter than the ones in POT-Au nanocomposite (Figure 6E). Although these shorter and entangled NFs have larger nanopores among them, they were managed to wrap most of the Cu NP clusters (~500 nm avg.) within the nanocomposite matrix (Figure 6E and F).

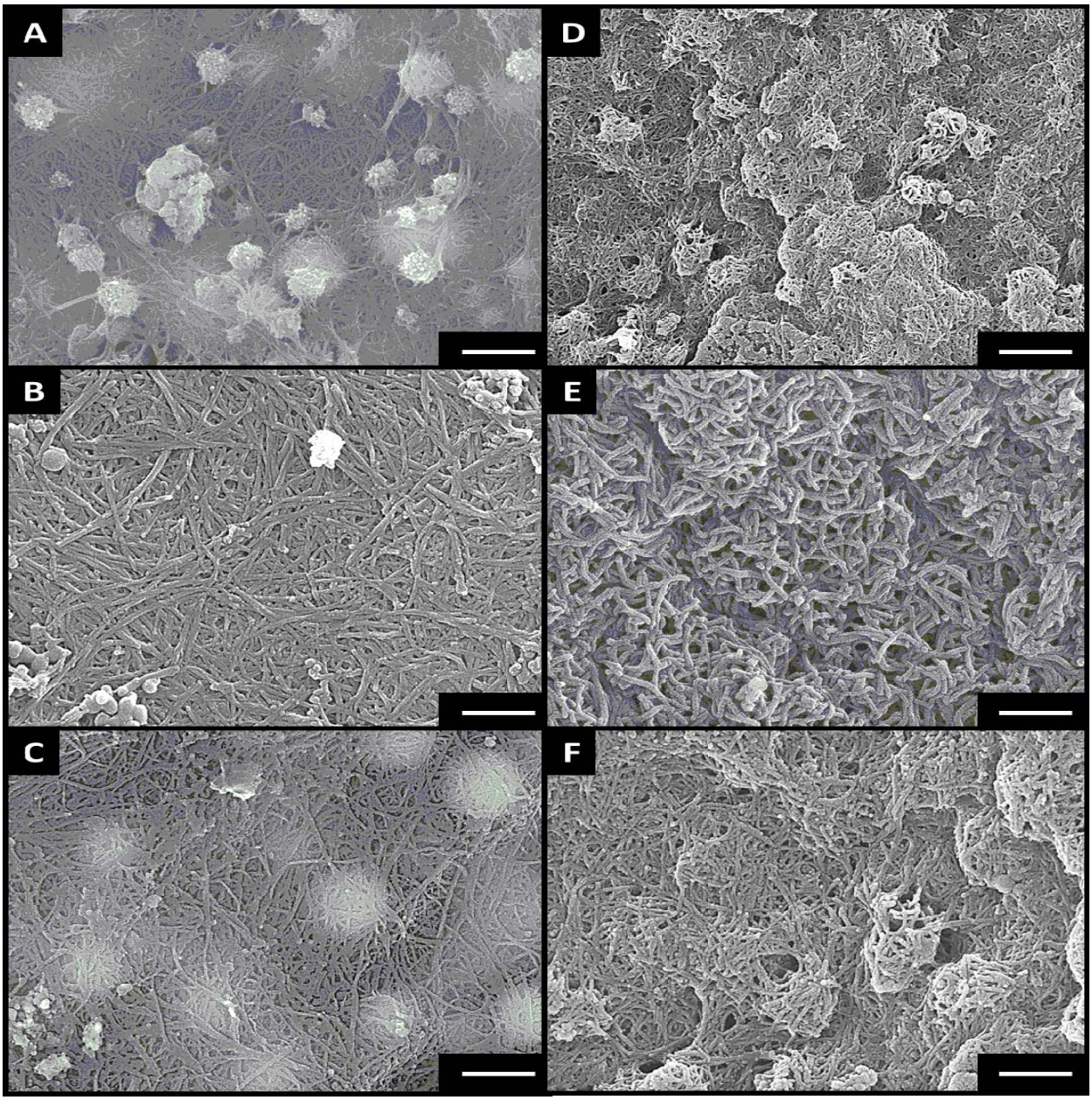

Figure 6. SEM images of (A, B, C) POT-Au nanocomposite; (B and C) zoomed-in views of the fibrous POT phase and Au NPs embedded into POT NFs. (D, E, F) POT-Cu nanocomposite; (E and F) zoomed-in views of the fibrous POT phase and Cu NPs covered by POT NFs, respectively. (Scale bars; A, B, C, E, F: 100 nm, D: 1 μm)

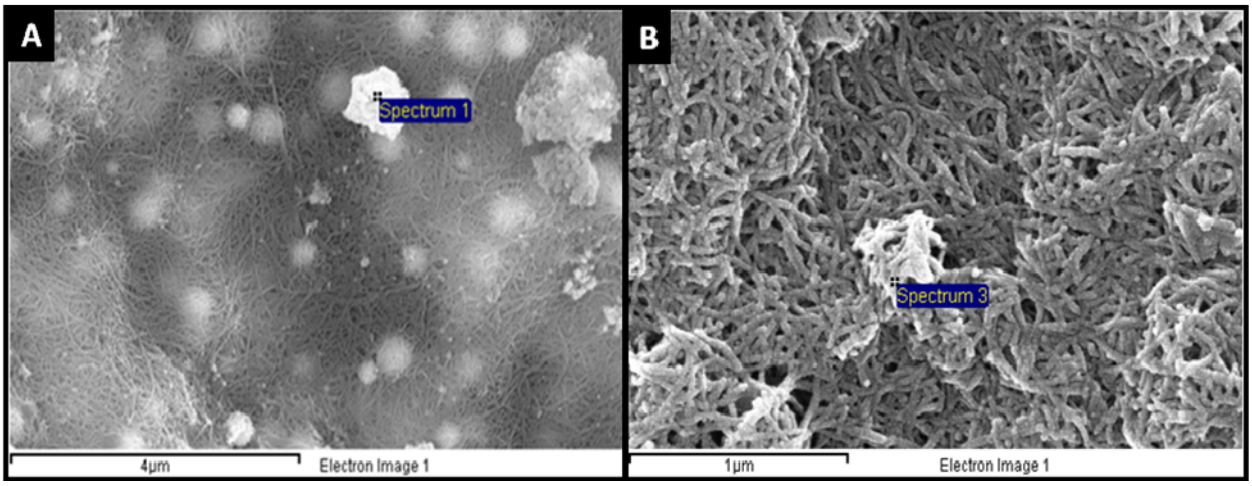

Figure 7. SEM images of; (A) Au, (B) Cu NP clusters in POT-Au/Cu nanocomposite network matrices

All these obvious morphology differences between Au and Cu systems would primarily affect their electrochemical properties, which would be explained in details along the following sections.

Table 1. Summary of the EDX results from the spectra in Figure 7

Systems	C	N	O	V	Au / Cu	Total
V_2O_5/o-toluidine/AuCl	-	-	3.94	-	96.06	100
V_2O_5/o-toluidine/$CuCl_2$	-	-	19.42	-	80.58	100

In order to have a more clear idea about the morphological properties of POT-Au/Cu nanocomposite networks, they were further investigated by HR-TEM. Similar with the SEM results, Au NPs with average diameters of 10-25 nm can be seen as homogenously encapsulated within the densely packed POT NF network (Figure 8A). Single Au NP decorated, long and straight POT NFs with ~20 nm average diameters can be observed in Figure 8B. The particle size distribution (PSD) of single-crystalline Au NPs within the nanocomposite network is

majorly (80%) around 6-10 nm (Figure 8C, 9A and 10A) and they have an average lattice fringe spacing of 0.236 nm, which is in good accordance with the previous literature (Figure 8C inset).[41]

On the other hand, Cu NPs exhibited a space-confined concentrated distribution within the POT NFs network.[40] Here, the size distribution of the Cu rich sites (NPs and clusters) within the nanocomposite structures ranges between 50-300 nm (Figure 8D). Cu NP decorated, web-like structure of POT NFs in this nanocomposite can be observed in Figure 8E. In addition, the difference in morphology between POT-Au and POT-Cu nanocomposites, in terms of NF length and thickness (~25 nm avg.), can be easily distinguished from the Figures 8B and E. Here, the discrepancy between the sizes of POT NFs in SEM and HR-TEM images can be attributed to the ultra-sonication process that was applied for sample preparation purposes. Again in perfect correspondence with the literature, the average lattice fringe spacing of single Cu NPs within the nanocomposite matrix is 0.21 nm (Figure 8F inset) indicating the presence of discrete crystalline domains inside them.[42] However, the SAED patterns of Cu NPs indicate that they are not perfect crystals (Figure 10B), but instead they are composed of smaller NPs with a major PSD (60%) ranging between 17-21 nm (Figure 8F and 9B). Commonly in these two systems, Au/Cu NPs tend to form clusters during the synthesis reactions due to their high surface energies, but they still keep their "particle" presence on those clusters probably because of their electrochemical interactions with POT NFs.[40] Furthermore, similarly formed NP clusters are expected to possess and exhibit superior size-dependent electrocatalytic properties owing to their NPs' narrow PSD and facet compositions.[40]

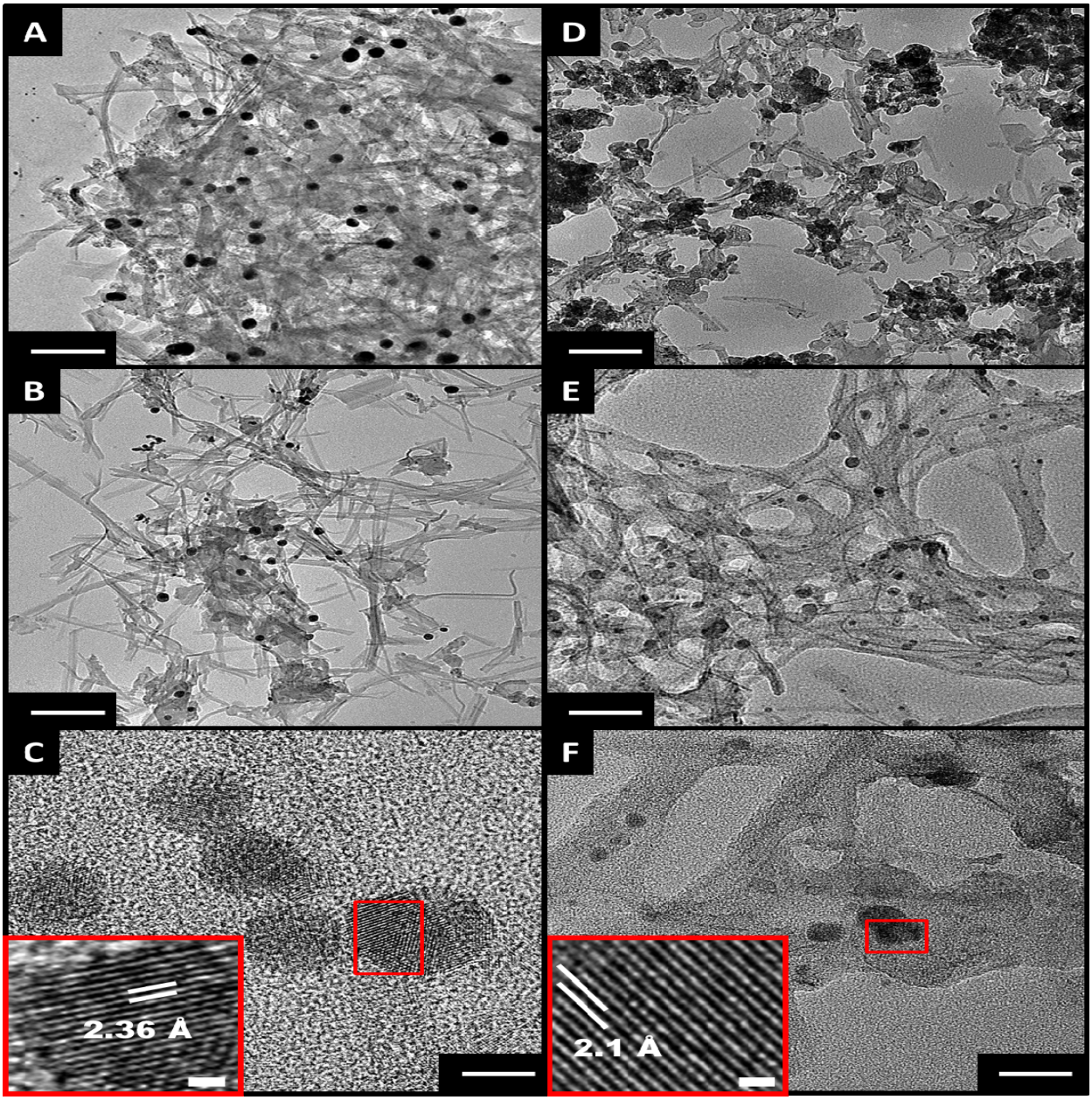

Figure 8. HR-TEM images of (A, B, C) POT-Au nanocomposite and (D, E, F) POT-Cu nanocomposite. Inset (C and F) are the zoomed-in views of the crystal lattice spacing in single Au and Cu NPs, respectively. (Scale bars; A: 100 nm, B, D: 200 nm, C: 5 nm, E: 50 nm, F: 20 nm)

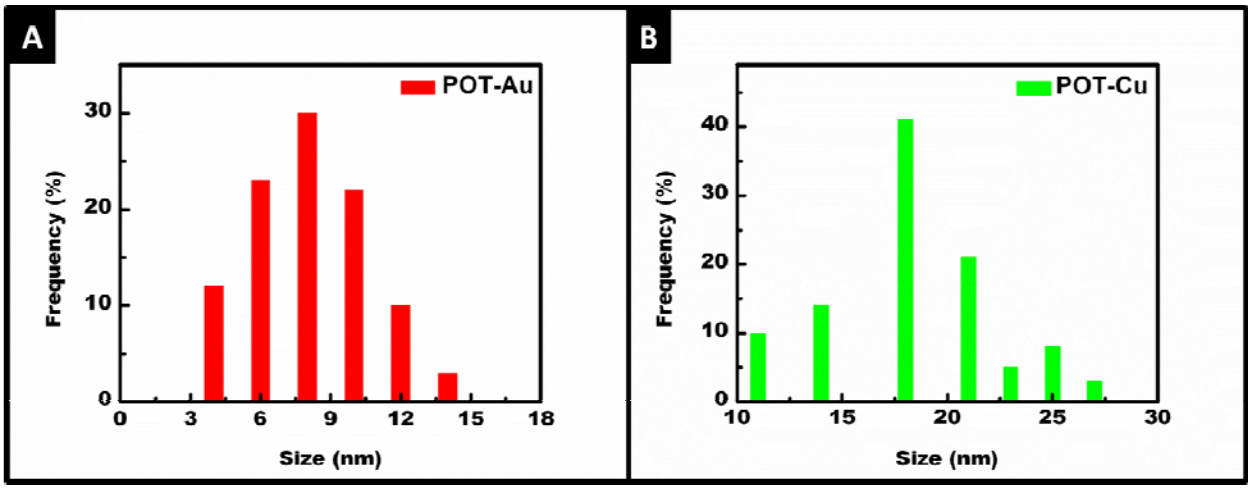

Figure 9. Particle size distribution (PSD) analysis graphics of; (A) POT-Au, (B) POT-Cu nanocomposites

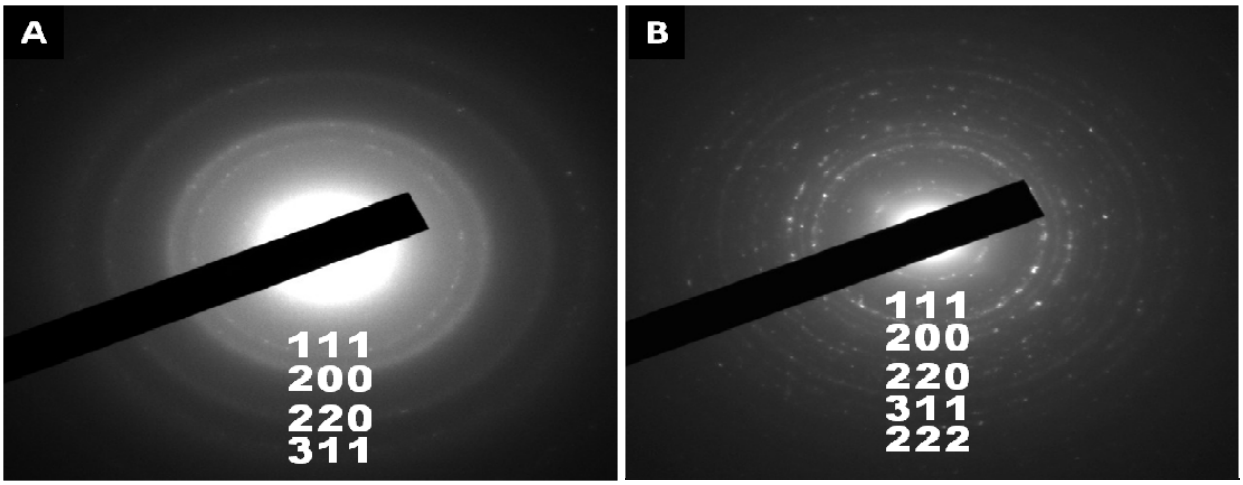

Figure 10. SAED patterns of; (A) single crystalline Au, and (B) oxide form of Cu NPs in POT-Au/Cu nanocomposite samples with characteristic diffraction rings from {111}, {200}, {220}, {311} and {222} reflections represented in their face-centered cubic (fcc) structures

After the completion of the nanocomposites' morphology confirmation through different electron microscopy techniques, their further structural characterizations; including the thermal,

spectroscopic, crystallographic and optical analyses were done by using different techniques. First, POT NFs and POT-Au/Cu nanocomposites were heated from room temperature up to 800 ºC, (at a heating rate of 10 ºC/min, in O_2 atmosphere) for the complete burning of the samples. Figure 11A shows the TGA graphics obtained from these heating processes, according to which, there are three main temperature regions that these samples had gone through major weight losses. Here, the first major weight loss, observed up to 100 ºC, corresponds to the loss of water molecules/moisture that exists in the samples.[5,14] The secondary weight loss, observed up to 250 ºC, can be attributed to the loss of dopants and low molecular weight oligomers that are attached to the primary POT chains.[5,14] The third major weight loss, observed between 250-450 ºC, took place due to the decomposition of primary POT backbone in each nanocomposite sample.[5,14] For the nanocomposite samples, there is an extra weight loss occurred around 550 ºC which is probably due to the decomposition of complex structures that were formed during the very early stages of the synthesis reactions at the interface of POT NFs and Au/Cu NPs (Figure 11A inset). Based on these thermograms, it can be summarized that; (i) the thermal stability of both nanocomposite samples are much better than that of pure POT NFs, and (ii) the loading of metal NPs in both nanocomposite samples are close to each other (36.5% Cu vs. 44.3% Au). These would be mainly because of either the electrochemical charge transfer interactions between Au/Cu NPs-amine/imine groups in POT NFs or due to the primarily mentioned synergistic effect between these two counterparts, which would have positive contributions to the overall nanocomposite properties.[5,14,40]

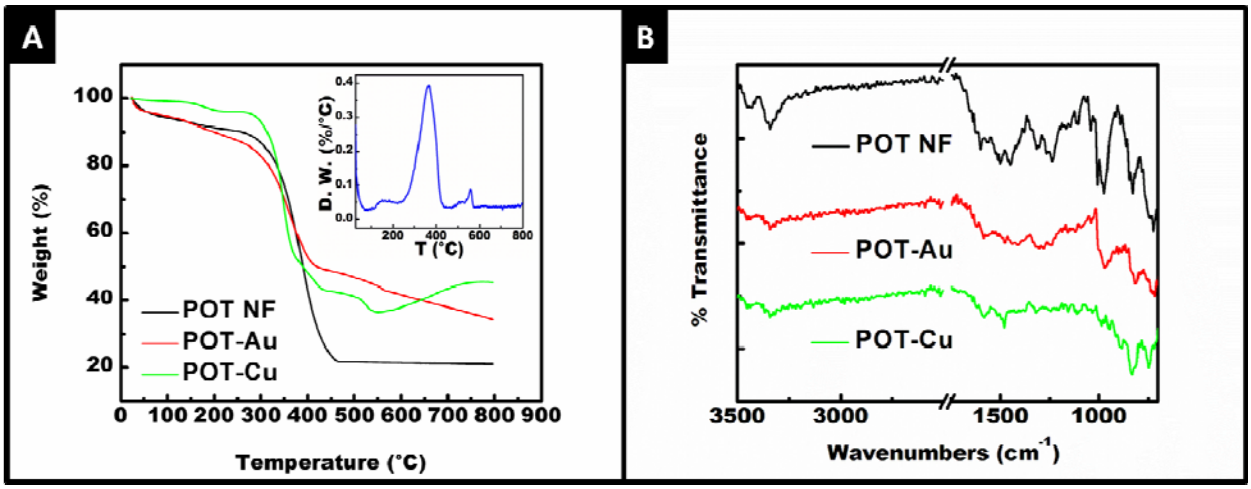

Figure 11. (A) TGA thermograms (Inset: derived weight graphic), (B) FT-IR spectra of POT NFs and POT-Au/Cu nanocomposites

The FT-IR spectra of the pristine POT NFs and POT-Au/Cu nanocomposites are shown Figure 11B. This characterization was applied to confirm the functional groups of doped POT via locating and comparing its characteristic peaks and their intensities represented in nanocomposite samples' spectra.[5] The spectrum belongs to the POT NFs exhibits the following characteristic peaks of N-H stretching vibration at 3430 cm^{-1}, and C-H stretching of the aromatic ring at 3340 cm^{-1}.[43] Additionally, the characteristic peaks from the C=C stretching of the quinoid and benzoid rings in POT NF chains can be seen at 1597 cm^{-1} and 1500 cm^{-1}, respectively.[44] Also, characteristic peaks of C-N stretching of secondary aromatic amine at 1315 cm^{-1},[12,14] C-C or C-N stretching and in plane C-H bending modes at 1210 and 1155 cm^{-1},[5,14,21] -N-quinoid-N- at 1107 cm^{-1},[5,14] and lastly C-H in plane vibration of the quinoid rings at 1005 cm^{-1},[5,14] can be observed from the same spectrum. When the POT-Au/Cu nanocomposites' spectra are observed; it is easy to realize the broadening/overlapping features, intensity changes[40] and slight shifting[5,14] occurred on the above mentioned characteristic POT peaks. The major reasons for these changes

can be; (i) the previously mentioned electrochemical charge transfer interactions between the highly conductive Au/Cu NPs and nitrogen rich sites on POT chains,[14] and (ii) low intra/intermolecular chain interactions among POT NFs due to the low polymerization degree, which was primarily triggered by metal salts with low oxidative potential, e.g. $CuCl_2$.[40]

The XRD patterns of the POT NFs and POT-Au/Cu nanocomposites are shown in Figure 12A. Two broad and distinctive characteristic POT peaks can be seen at NF diffractogram at $2\theta = 25°$ and 45°, respectively. [5,14,15,21] However, in POT-Au/Cu nanocomposite samples' diffractograms, the shoulder at 25° is significantly broadened and diminished, and the other one at 45° is disappeared due to getting overlapped with Au/Cu NP characteristic peaks.

Furthermore, when the POT-Au/Cu nanocomposites' XRD diffractograms are examined; there are two sharp and three small peaks can be noticed at $2\theta = 38°$, 44°, 64°, 77°, 81° and at $2\theta = 43°$, 50°, 74°, 89°, 95° representing the Bragg's reflections from {111}, {200}, {220}, {311} and {222} planes of Au[5,9,11,26] and Cu (oxide form)[43,45] NPs, respectively. These results are in very good agreement, both with the previously explained TEM results in Figure 8C and F insets, the SAED patterns in Figure 10, and the standard literature data, e.g. JCPDS No. 4-784 and 4-836,[42,46] which are strongly supporting the presence of face-centered cubic (fcc) metal NPs with dominant {111} lattice planes in POT-Au/Cu nanocomposite samples.[41,42]

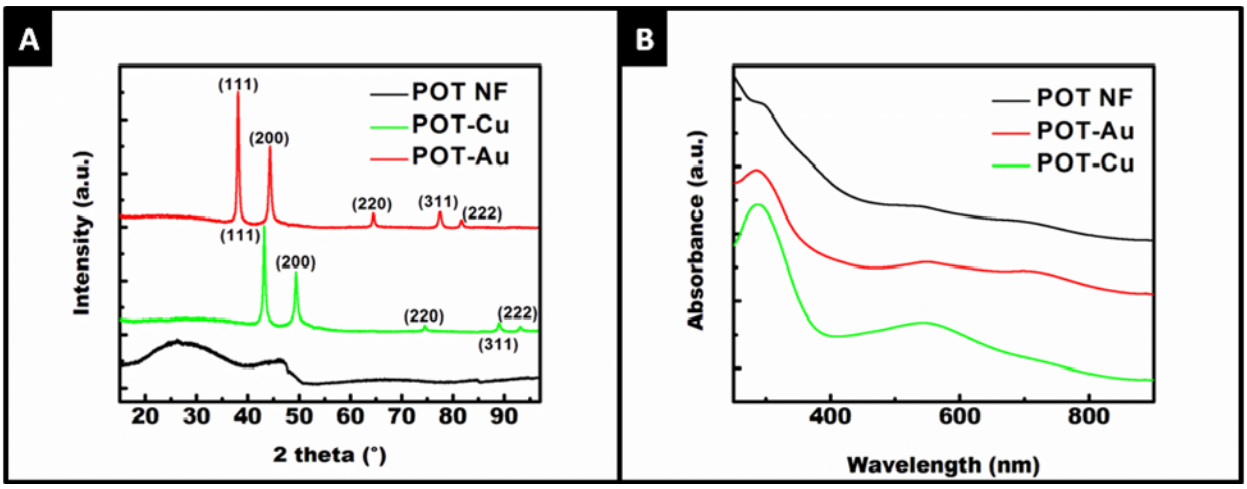

Figure 12. (A) XRD diffractograms and (B) UV-Vis spectra of POT NFs and POT-Au/Cu nanocomposites

Lastly, the optical properties of POT NFs and POT-Au/Cu nanocomposite samples were characterized by UV-Visible spectroscopy (Figure 12B). Characterization of this property is very important to ascertain the formation mechanism of both NFs and the nanocomposites, i.e. the electronic/interfacial interactions that occurred between POT NFs and Au/Cu NPs during the synthesis reactions.[12,44] There are three peaks, located around 315-320 nm,[3,4,6] 550-600 nm,[11,12,16] and 700-750 nm wavelengths,[11,47,48] can be observed at POT NFs' optical spectrum. Among those peaks; the first one represents the π-π* transition/excitation[10-12] centered on the benzoid rings (amine segments)[15,16] of the POT chain,[22,47] the second one represents the n-π* transition from the nonbonding nitrogen lone pair to the conduction (π*) band,[16] and the last one is related to the polaron band of POT.[47,48] According to these results POT NFs are found to be in their "emeraldine base" forms. However, there was a high possibility of blue shift occurrence in those characteristic peaks due to the introduction/presence of $-CH_3$ groups on POT chains, whose effect was discussed at the introduction part.[3,47,48] When POT-Au nanocomposite's optical

spectrum is analyzed, the presence of a distinct characteristic Au NP surface plasmon resonance band[5,10] around 520-570 nm wavelength[26,37] can be observed. Similarly, due to the plasma oscillation on the Cu NPs surface in POT-Cu nanocomposite structure, a characteristic peak around 570-600 nm wavelength can be observed at the corresponding spectrum.[4,22] The intensity of these two peaks depends on the; (i) size/shape of NPs, (ii) electronic nature of the nanocomposite, e.g. the dielectric constant, and (iii) the strength of the interactions between NPs.[5] On the other hand, their intensity is reversely proportional with the amount of polymeric phase in the nanocomposite structure, which is determined by the oxidative potential of the metal salts used the nanocomposite synthesis reaction section.

1.3.3 Formation mechanism of POT-Au/Cu nanocomposites

The successful one-step synthesis of POT-Au/Cu nanocomposite networks has been readily verified through all the above mentioned characterization results, which are also supported by the previous literature. Electrochemical dynamics of these synthesis reactions are explained in details along with the open circuit potential measurements (Figure 5). Additionally, here, a plausible formation mechanism/sequence for these nanocomposites is proposed as follows. First, o-toluidine monomers are adsorbed and get partially oxidized on the surface of homogenously dispersed, reactive V_2O_5 sol-gel NF seeds in the aqueous suspensions.[18] Such oxidative interactions caused a noticeable darkening in reaction media colors.[49] As the reactions proceeded, nanofibrillar o-toluidine structures were generated in oligomer forms via mirroring the V_2O_5 NF seeds' morphology.[13,40] When the metal salts were added, rapid formations of the POT-Au/Cu precipitates, along with the fully darkening of the reaction media colors, were observed.[13,49] At this stage, the presence of electron-donating "-CH_3" groups along the OT oligomer chains facilitated the relay of electrons through the nitrogen lone pairs of the amine

groups, and triggered the instantaneous formation of the electrostatic bonds with Au^{+} or Cu^{2+} cations. These electrostatic attachments were lead to the formations of reactive (H_3C-C_6H_4-$N^{(\cdot+)}H_2$) species which would later undergo oxidative polymerization. Here, each step of the polymerization was involved an electron release, which was used to reduce the above mentioned metal cations and form their corresponding atoms. Eventually, these atoms tend to unify and form their NPs/clusters which were finally got stabilized within the as-grown POT NF matrix. Moreover, this formation mechanism/sequence of the POT-Au/Cu nanocomposites ensures the development of a substantial contact between metal NPs and CP NFs.[4-6,17,22,40]

1.3.4 Electrochemical characterization of POT-Au/Cu nanocomposites

Due to their nanocomposite network structure that has been explained in details so far, the as-obtained POT-Au/Cu nanocomposites with porous CP NF matrices and within homogenously distributed metal NPs are expected to exhibit superior electrocatalytic performance. Highly efficient electron transfer between the catalytically active centers (Au/Cu NPs) at nanocomposites and the bulk graphite working electrode (WE) was achieved through the formation of POT NF bridges via colloidal graphite paste attachment. Also, the confinement of evenly distributed/embedded metal NPs within POT NFs network, like a sheath, ensured the long-term stability of these nanocomposites through the prevention of potential metal NP poisoning at their final areas of use.[40] Since; (i) the effectively electron transferable structure and (ii) long-term stability are the two major issues that need to be solved in electrochemical applications, i.e. biosensory[24,25,40] or methanol fuel cell,[23] proper addressing of both issues via the nanocomposites synthesized within this study will be appreciated. Thus, at this stage, POT-Au/Cu nanocomposite-based non-enzymatic glucose sensors were prepared on modified graphite

WEs (POT-Au/Cu-G) and their electrochemical properties were characterized with different techniques.

The cyclic voltammograms (CVs) of POT-Au/Cu-G electrodes within 0.1 M aq. NaOH electrolyte at different glucose concentrations are shown in Figure 13. Based on the results, both electrodes exhibit the characteristic behaviors of Au/Cu NPs in their structures. The typical major regions of; hydrogen adsorption region (-0.8 V to -0.4 V), double layer region (-0.4 V to 0 V) and the oxide formation region (0 V to 0.6 V) can be observed from the corresponding CVs.[35,37] Upon the addition of glucose into the electrolyte, there were three peaks appeared along the anodic scan of POT-Au-G electrode's CV, located at -0.55 V, -0.25 V and 0.3 V, respectively (Figure 13A). Similarly, three anodic peaks centered at -0.6 V, -0.25 V and 0.5 V were appeared at POT-Cu-G electrode's CV, as well (Figure 13B).

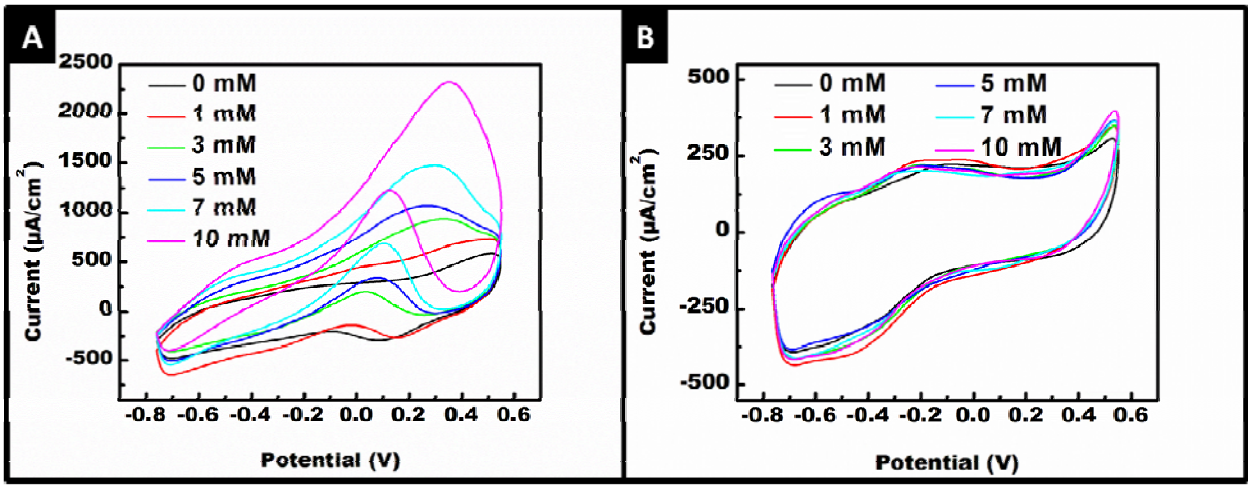

Figure 13. CVs of; (A) POT-Au-G, and (B) POT-Cu-G electrodes with increasing glucose concentrations (0-10 mM) in 0.1 M aq. NaOH electrolyte at a scan rate of 20 mV/s

All of these three anodic peaks, with apparently broad shapes, were depicting the complex electrochemical oxidation mechanism of glucose on the surface of corresponding electrodes used for this application.[28,29,35-37] Among those peaks, the first one around -0.6 V to -0.5 V was representing the chemisorption of glucose and following adsorbed intermediate formations on the surface of electrodes. In general, there should be a decrease in the current density after this chemisorption.[35] However, in this case, the continuous increase in both electrodes' current densities indicates the unsaturated adsorption of glucose on the POT-Au/Cu-G electrodes, which is most probably due to their ultra-high surface areas.[40] The following peak, appeared around -0.3 V to -0.2 V, was formed upon the catalytic oxidation of the adsorbed intermediates by the as-generated OH adsorbed atoms (ad-atoms) on the Au/Cu NPs surface.[29,35-37] As a result of this oxidation process, reactive sites on the Au/Cu NPs became available for the direct oxidation of glucose, which would lead to the formations of the last peaks at 0.3 V on POT-Au-G electrode's CV and at 0.5 V on POT-Cu-G electrode's CV, respectively.[28,36,37] As the anodic scan was proceeded beyond these potentials, formations of thick Au and Cu oxide layers took place and prevented the further oxidation of glucose, which resulted as a sharp decrease in current densities on both electrodes' CVs.[40]

It was also possible to identify three peaks along the cathodic scans of the same CVs. Here, the ones on the POT-Au-G electrode's CV were located around 0.4 V to 0.1 V, -0.25 V and -0.7 V (Figure 13A), whereas the ones on POT-Cu-G electrode's CV were located at 0.45 V to 0.3 V, -0.45 V and -0.7 V, respectively (Figure 13B). Among those peaks, the first ones were representing the induction periods for the reduction of pre-formed Au/Cu surface oxides, which were followed by the main reduction peaks at -0.25 V for POT-Au based electrode and the other one at -0.45 V for the POT-Cu based electrode.[28,29,37] The final peaks located at -0.7 V were both

ascribed to the reduction/desorption of the pre-adsorbed oxidized intermediates on the POT-Au/Cu-G electrode surfaces. The overall summary of the anodic/cathodic peaks' locations on these CVs was indicating reversible electrode characteristics for the glucose oxidation process, whose electrochemical kinetics were controlled by the surface adsorption of glucose molecules.[28,40]

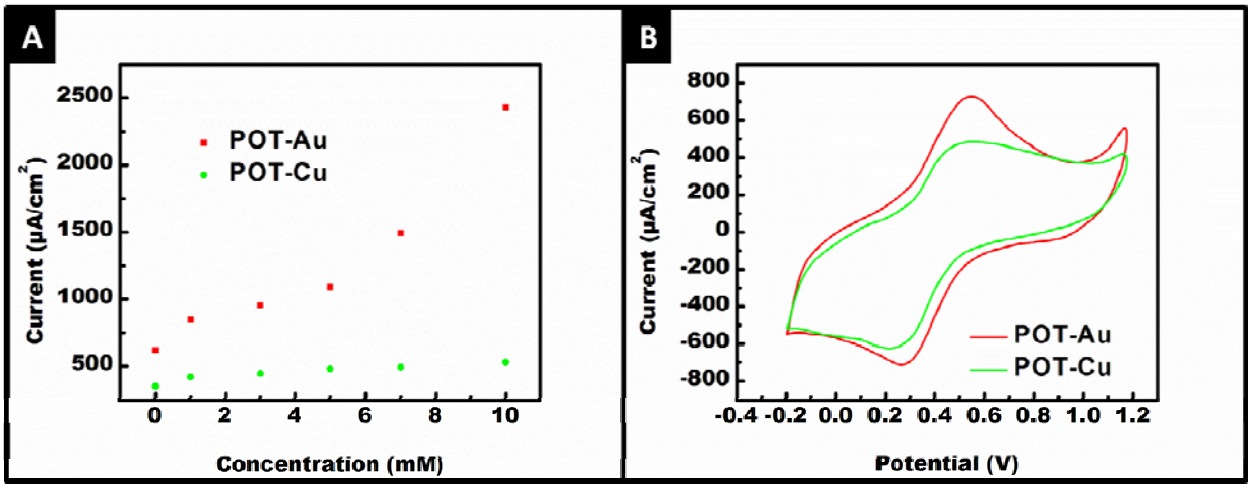

Figure 14. (A) Summary plots of the POT-Au/Cu-G electrodes' CV peak current densities, and (B) CVs of POT-Au/Cu-G electrodes in 0.1 M aq. H_2SO_4 electrolyte at a scan rate of 10 mV/s

Also, the linear relationship between the increased CV peak current densities and the glucose concentration in the electrolytes can be readily observed, especially for the POT-Au based electrode, as a result of the rapid and highly stable electrode responses generated during the oxidation of glucose in alkaline media (Figure 14A).[28,40] Similarly to this phenomenon, the red shift occurred on the glucose oxidation peaks can be attributed to the slower electron transfer properties of POT NFs (compared to the metal NPs) in both nanocomposite electrode structures.[40] However, presence of these NFs was synergistically contributing to the

electrocatalytic performance of POT-Au/Cu based electrodes via either increasing the active surface area or securing the Au/Cu NPs from poisoning and electrochemical property loss.[28,36]

The summary of the peak current densities for the glucose oxidation peaks on the POT-Au/Cu-G electrodes' CVs is shown in Figure 14A. Here, larger peak current densities as well as more obvious responses towards the glucose oxidation can be observed from the POT-Au-based electrode. This result is also in very good agreement with the previously explained SEM/HR-TEM characterization results of the nanocomposites, and indicating the superior electrocatalytic performance of the POT-Au-based electrode than the POT-Cu-based one, with respect to its advantageous morphological features. CVs of the POT-Au/Cu-G electrodes in 0.1 M aq. H_2SO_4 electrolyte in Figure 14B are also supporting the above mentioned phenomenon. Here, the overall electrochemical behaviors of POT-Au/Cu nanocomposite-based electrodes were investigated. Since, the POT network in POT-Au nanocomposite was composed of thinner NFs which were more densely packed with smaller intra-fiber pores and metal NPs; this nanocomposite was expected to exhibit better electrochemical properties compared to the POT-Cu nanocomposite, as shown in Figure 14B. Thus, apparently larger CV area and sharper characteristic POT peaks with overlapping features (most probably due to the presence of metal NPs) were both observed from the POT-Au-G electrode's voltammogram.[3,32,50]

After the verification of the excellent non-enzymatic glucose sensing properties of POT-Au/Cu nanocomposites, the linear operation range of the POT-Au-G electrode was also determined by recording its steady-state amperometric responses towards the successive addition of glucose at certain periods (Figure 15).[32] A well-defined and highly stable amperometric response can be observed for the POT-Au-G electrode upon successive additions of 1 mM glucose at an interval of 1 min., until 30 mM glucose concentration was reached in the

electrolyte (Figure 15A).[28] For each addition of 1 mM glucose, the time to achieve the steady-state plateau for the electrode response was no more than 5 s, which was indicating the rapid and sensitive glucose detection shown by this electrode.[28,40]

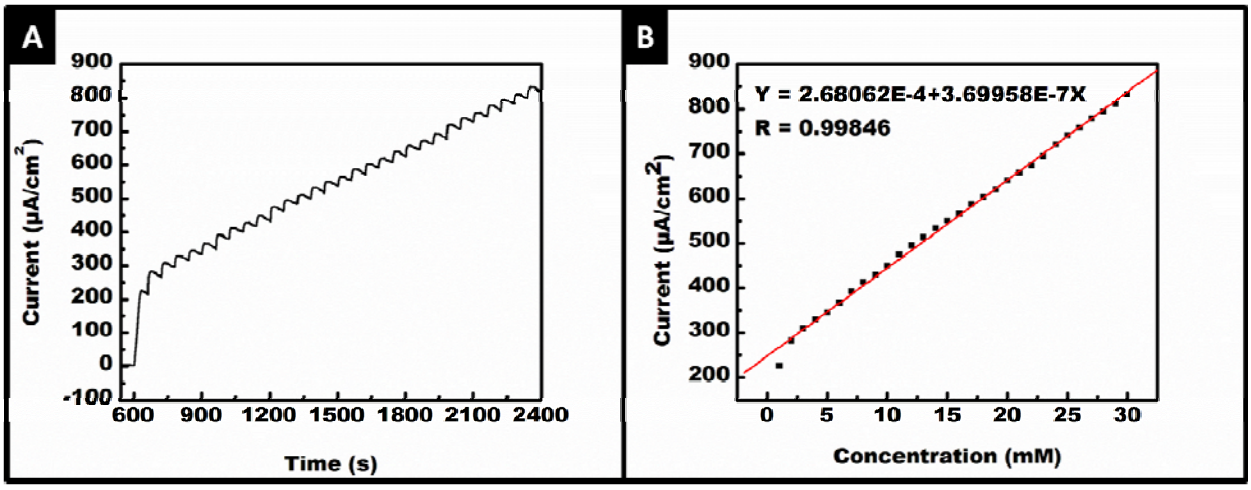

Figure 15. (A) Amperometric responses of the POT-Au/Cu-G electrode upon successive additions of 1 mM glucose per minute up to 30 mM in 0.1 M aq. NaOH electrolyte at an applied potential of 0.1 V, (B) Corresponding calibration curve for the electrode response

The corresponding calibration curve for the POT-Au-G electrode indicates that there is a linear dependence between the oxidation current and glucose concentration (Figure 15B).[27-29,32] According to the calculations based on this curve; the correlation coefficient was R = 0.99846, the concentration limit of the electrode was ~37 μA/mM*cm^2 and its detection limit (at signal/noise = 3) was ~0.027 μM. The overall glucose sensing performance of POT-Au-G electrode with rapid responses, very high detection limit and wide linear range is quite competitive with both the previous and current non-enzymatic glucose sensors in the literature.[27-29,40] Here, the wide linear range can be attributed to the previously mentioned morphological

advantages of this electrode, i.e. (i) larger electroactive site due to the presence of smaller size Au NPs/clusters, (ii) ultra-high surface area for more glucose adsorption/oxidation and (iii) superior electrocatalytic performance due to the effective electron transfer process between Au NPs and POT NFs. Thus, when combined this property with its high sensitivity and low detection limit, POT-Au nanocomposite will be one of the major materials of preference for the next generation non-enzymatic glucose sensors that would be used for either physiological level or clinically relevant detection of glucose.[28,40]

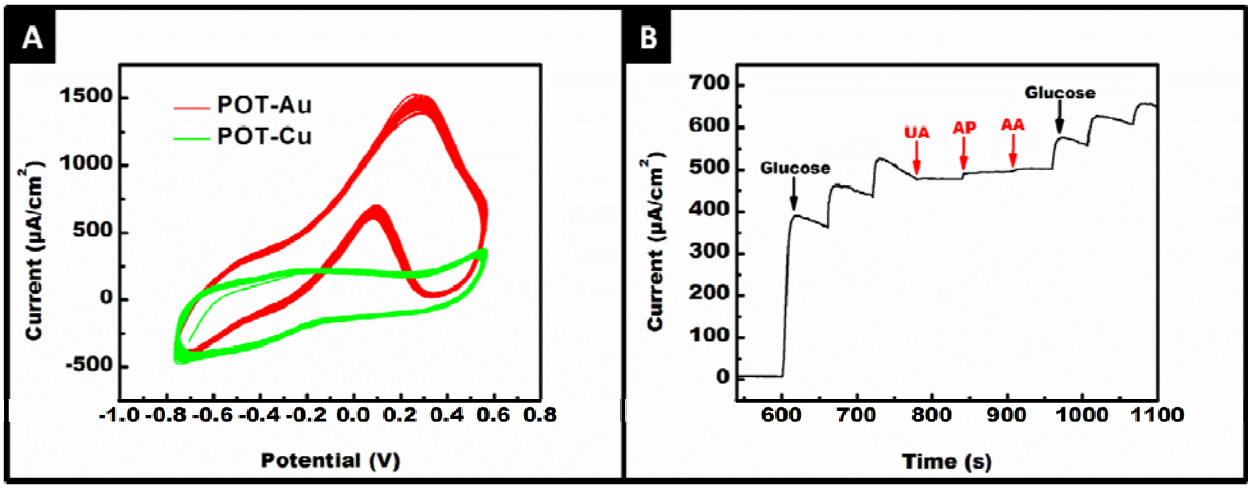

Figure 16. (A) Stacked CVs of the POT-Au/Cu-G electrodes in 0.1 M aq. NaOH solution containing 5 mM glucose at a scan rate of 20 mV/s (50 cycles), (B) Chronoamperometric responses of the POT-Au-G electrode upon successive additions of 5 mM glucose, 0.02 mM UA, 0.1 mM AP and 0.1 mM AA into 0.1 M aq. NaOH electrolyte at an interval of 1 min., and applied potential of 0.1 V

Lastly, the repetitive cycling stability and the anti-interference properties of POT-Au/Cu-G electrodes were characterized (Figure 16). Figure 16A shows the stacked CVs of both

electrodes obtained from their 50 repetitive cycles in 0.1 M aq. NaOH electrolyte containing 5 mM glucose. Here, very slight changes/shifting that occurred both in the overall voltammogram shapes and the characteristic peak locations were indicating the high electrocatalytic stability of the POT-Au/Cu nanocomposites on the electrodes. This can be attributed to the substantial structure of these nanocomposites, which was preserved very well during the repetitive cycles and prevented the possible catalyst dissolutions/aggregations.[40] In addition, the unchanged glucose sensing property of these electrodes, in the presence of a well-known poisoning agent for metal NP catalysts at its physiological level, e.g. chloride (Cl^-) ions,[29] is shown in Figure 17.

Selectivity of these electrodes towards glucose in the presence of common interfering reagents such as UA, AP and AA, which are generally co-exist with glucose in real physiological samples, was also evaluated (Figure 16B).[27-29] Thus, the chronoamperometric responses of the electrode was recorded upon the successive additions of 5 mM glucose and the above mentioned interfering agents into the electrolyte, at an interval of 1 min.

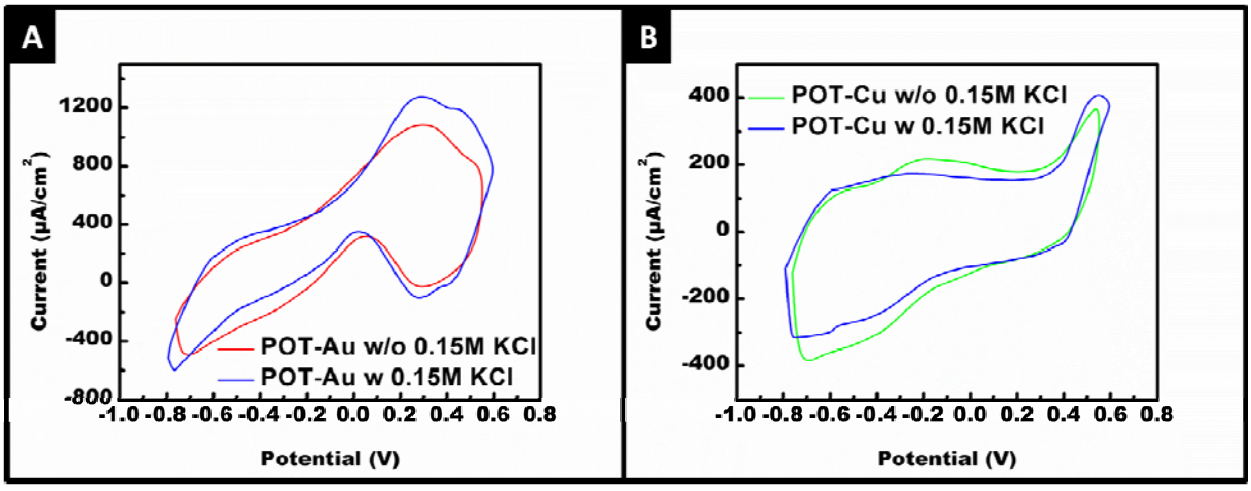

Figure 17. CVs of; (A) POT-Au-G, (B) POT-Cu-G electrodes in 0.1 M aq. NaOH solution containing 5 mM glucose, before and after (blue lines) the addition of 0.15 M KCl

It was clearly observed from the results that, the electrode exhibited distinct anti-interference property, since negligible current responses were caused by the reagents.[37-39] Moreover, stable current responses towards glucose addition were still retained even after the interfering agents additions (Figure 16B).[40] The highly selective characteristic of the nanocomposite based electrodes can be given to two things as follows; (i) the previously mentioned, effective electron transfer process between POT NFs and Au/Cu NPs made the privileged oxidation of glucose possible at low potentials, rather than the other interfering reagents, and (ii) the protective POT NFs wrap around the Au/Cu NPs would limit the accessibility of the interfering reagents to the surface of metal NPs, at which the oxidation takes place.[40]

1.4 Conclusions

Inspiring from the certain innovations in nanotechnology and increasing demands from the market; in this study, POT NFs and Au/Cu NPs were facilely synthesized in nanocomposite network forms through a one-step seeding polymerization reaction and a redox/complexation process that occurred between monomers and corresponding metal salt cations in aqueous media at room temperature.

The as-synthesized nanocomposites exhibited; (i) unique morphological features and substantial integrity that secure the homogenously distributed Au/Cu NP catalysts within POT NFs network, along with (ii) superior electron transfer property between these counterparts, which were all turned out to be advantageous for their final use as non-enzymatic glucose sensors. Also, the four major requirements of a typical glucose sensor, namely; (i) high sensitivity for glucose (~0.027 μM at S/N = 3), (ii) wide linear operation range (R = 0.99846 up

to 30 mM and 37 μA/mM*cm^2 limit), (iii) multiple cycling stability (up to 50 cycles) and (iv) high selectivity (in the presence of UA, AA, AP and Cl^- at their physiological levels) were successfully achieved by the electrodes prepared with those nanocomposites.

It is certain that these sophisticatedly engineered hybrid nanocomposite network structures will soon become the materials of preference as the active electrodes for the applications of next generation non-enzymatic glucose sensors.

1.5 References

(1) Shirakawa, H.; Louis, E. J.; Macdiarmid, A. G.; Chiang, C. K.; Heeger, A. J. *Journal of the Chemical Society-Chemical Communications* 1977, 578-580.

(2) MacDiarmid, A. G. *Angewandte Chemie-International Edition* 2001, *40*, 2581-2590.

(3) Wan, M.; Yang, J. *Synthetic Metals* 1995, *73*, 201-204.

(4) Mallick, K.; Witcomb, M. J.; Scurrell, M. S. *Materials Science and Engineering B-Solid State Materials for Advanced Technology* 2005, *123*, 181-186.

(5) Reddy, K. R.; Lee, K. P.; Gopalan, A. Y. *Journal of Nanoscience and Nanotechnology* 2007, *7*, 3117-3125.

(6) Mallick, K.; Witcomb, M. J.; Scurrell, M. S. *Journal of Materials Science* 2006, *41*, 6189-6192.

(7) Han, J.; Wang, L.; Guo, R. *Macromolecular Rapid Communications* 2011, *32*, 729-735.

(8) Blaz, E.; Pielichowski, J. *Molecules* 2006, *11*, 115-120.

(9) Jiang, S.; Chen, J. Y.; Tang, J.; Jin, E.; Kong, L. R.; Zhang, W. J.; Wang, C. *Sensors and Actuators B-Chemical* 2009, *140*, 520-524.

(10) Reddy, K. R.; Sin, B. C.; Ryu, K. S.; Kim, J. C.; Chung, H.; Lee, Y. *Synthetic Metals* 2009, *159*, 595-603.

(11) Han, J.; Liu, Y.; Guo, R. *Journal of Applied Polymer Science* 2009, *112*, 1244-1249.

(12) Choudhury, A. *Materials Chemistry and Physics* 2011, *130*, 231-236.

(13) Zhang, X. Y.; Goux, W. J.; Manohar, S. K. *Journal of the American Chemical Society* 2004, *126*, 4502-4503.

(14) Reddy, K. R.; Lee, K. P.; Lee, Y.; Gopalan, A. I. *Materials Letters* 2008, *62*, 1815-1818.

(15) Ding, S. H.; Lu, X. F.; Zheng, J. N.; Zhang, W. J. *Materials Science and Engineering B-Solid State Materials for Advanced Technology* 2006, *135*, 10-14.

(16) Bavastrello, V.; Carrara, S.; Ram, M. K.; Nicolini, C. *Langmuir* 2004, *20*, 969-973.

(17) Mallick, K.; Witcomb, M. J.; Dinsmore, A.; Scurrell, M. S. *Langmuir* 2005, *21*, 7964-7967.

(18) Zhang, X. Y.; Manohar, S. K. *Journal of the American Chemical Society* 2005, *127*, 14156-14157.

(19) Liu, Z.; Zhang, X. Y.; Poyraz, S.; Surwade, S. P.; Manohar, S. K. *Journal of the American Chemical Society* 2010, *132*, 13158-13159.

(20) Liu, Z.; Liu, Y.; Poyraz, S.; Zhang, X. Y. *Chemical Communications* 2011, *47*, 4421-4423.

(21) Nyczyk, A.; Hasik, M.; Turek, W.; Sniechota, A. *Synthetic Metals* 2009, *159*, 561-567.

(22) Mallick, K.; Witcomb, M. J.; Scurrell, M. S. *European Polymer Journal* 2006, *42*, 670-675.

(23) Liu, Z.; Poyraz, S.; Liu, Y.; Zhang, X. Y. *Nanoscale* 2012, *4*, 106-109.

(24) Liu, Y.; Liu, Z.; Lu, N.; Preiss, E.; Poyraz, S.; Kim, M. J.; Zhang, X. Y. *Chemical Communications* 2012, *48*, 2621-2623.

(25) Liu, Z.; Liu, Y.; Zhang, L.; Poyraz, S.; Lu, N.; Kim, M.; Smith, J.; Wang, X. L.; Yu, Y. J.; Zhang, X. Y. *Nanotechnology* 2012, *23*, 335603.

(26) Lu, X. F.; Chao, D. M.; Chen, J. Y.; Zhang, W. J.; Wei, Y. *Materials Letters* 2006, *60*, 2851-2854.

(27) Zhang, X.; Wang, G.; Huang, Y.; Yu, L.; Fang, B. *Micro & Nano Letters* 2012, *7*, 168-170.

(28) Luo, J.; Jiang, S. S.; Zhang, H. Y.; Jiang, J. Q.; Liu, X. Y. *Analytica Chimica Acta* 2012, *709*, 47-53.

(29) Huang, T. K.; Lin, K. W.; Tung, S. P.; Cheng, T. M.; Chang, I. C.; Hsieh, Y. Z.; Lee, C. Y.; Chiu, H. T. *Journal of Electroanalytical Chemistry* 2009, *636*, 123-127.

(30) Clark, L. C.; Lyons, C. *Annals of the New York Academy of Sciences* 1962, *102*, 29-&.

(31) Hsu, C.-T.; Chung, H.-H.; Tsai, D.-M.; Fang, M.-Y.; Hsiao, H.-C.; Zen, J.-M. *Analytical Chemistry* 2009, *81*, 515-518.

(32) Ekinci, E. *Polymer Bulletin* 1999, *42*, 693-699.

(33) Updike, S. J.; Hicks, G. P. *Nature* 1967, *214*, 986-&.

(34) Yoshida, E.; Hyodo, T.; Shimizu, Y.; Egashira, M. *Sensor Letters* 2008, *6*, 916-919.

(35) Park, S.; Boo, H.; Chung, T. D. *Analytica Chimica Acta* 2006, *556*, 46-57.

(36) Kang, X. H.; Mai, Z. B.; Zou, X. Y.; Cai, P. X.; Mo, J. Y. *Chinese Chemical Letters* 2007, *18*, 189-191.

(37) Yan, W.; Feng, X. M.; Chen, X. J.; Hou, W. H.; Zhu, J. J. *Biosensors & Bioelectronics* 2008, *23*, 925-931.

(38) Feng, D.; Wang, F.; Chen, Z. L. *Sensors and Actuators B-Chemical* 2009, *138*, 539-544.

(39) Bai, Y.; Yang, W. W.; Sun, Y.; Sun, C. Q. *Sensors and Actuators B-Chemical* 2008, *134*, 471-476.

(40) Liu, Y.; Lu, N.; Poyraz, S.; Wang, X.; Yu, Y.; Scott, J.; Smith, J.; Kim, M. J.; Zhang, X. *Nanoscale* 2013, *5*, 3872-3879.

(41) Johnson, C. J.; Dujardin, E.; Davis, S. A.; Murphy, C. J.; Mann, S. *Journal of Materials Chemistry* 2002, *12*, 1765-1770.

(42) Hansen, P. L.; Wagner, J. B.; Helveg, S.; Rostrup-Nielsen, J. R.; Clausen, B. S.; Topsoe, H. *Science* 2002, *295*, 2053-2055.

(43) Shinde, V.; Sainkar, S. R.; Patil, P. P. *Corrosion Science* 2005, *47*, 1352-1369.

(44) Chabukswar, V.; Bhavsar, S.; Horne, A. *Chemistry & Chemical Technology* 2011, *5*, 37-40.

(45) Kumar, R. V.; Mastai, Y.; Diamant, Y.; Gedanken, A. *Journal of Materials Chemistry* 2001, *11*, 1209-1213.

(46) Wang, X.; Zhuang, J.; Peng, Q.; Li, Y. *Nature* 2005, *437*, 121-124.

(47) Wan, M.; Li, J. *Polymers For Advanced Technologies* 2003, *14*, 320-325.

(48) Borole, D. D.; Kapadi, U. R.; Mahulikar, P. P.; Hundiwale, D. G. *Journal of Materials Science* 2005, *40*, 5499-5506.

(49) Zhang, X. Y.; Manohar, S. K. *Journal of the American Chemical Society* 2004, *126*, 12714-12715.

(50) Raoof, J. B.; Ojani, R.; Hosseini, S. R. *Journal of Power Sources* 2011, *196*, 1855-1863.

CHAPTER 2

One-step Synthesis and Characterization of Polyaniline Nanofiber/Silver Nanoparticle Composite Networks as Antibacterial Agents

2.1 Introduction

Throughout the last several decades; (i) the emergence of more resistant strains of detrimental microorganisms[1] like bacterium, virus, mold, yeast and etc., (ii) the increased possibility for humans to get exposed to these different strains in their daily living/working environments and to get more frequently infected by them,[2] have been the major reasons behind all different studies with "antibacterial material" focus. Intensive research efforts have been spent for such studies and their relevant applications, in order to find out substantial solutions that are targeting to ensure a cleaner/healthier life for people by effectively using this materials.[3]

The diversity of the antibacterial materials used in such studies; including the renewable plant-based substances (tea extract,[2] chitosan[4-6]), noble/metal nanoparticles (NPs), oxides and their cations (copper,[6,7] zinc,[6,7] titanium,[6,8] platinum,[9] silver (Ag)[1,6-15] and gold[16]), conducting polymers (CPs) (polyaniline (PANI),[3,9,16-21] polyrhodanine,[22,23] polypyrrole[24]), N-halamines[6,25-27] and carbon nanotubes[28] etc., covers a very wide span. Among those materials, noble metal "Ag" has been the most sought-after,[29] commonly engineered and commercialized[13,14] one by the researchers, due to its distinguishing electrical, optical, long-term stable chemical and catalytic properties.[6,8,30-32] In addition to its other uses in surface-enhanced Raman scattering (SERS),[8]

photonic crystals,[33] catalysis,[14] nano-electronic luminescent devices,[29] biochemical tagging,[33] food packaging,[13] sensory[20] and so on,[32-37] Ag has particularly been known and utilized as a powerful antibacterial agent[2,34-37] in either its elemental, NP or cationic salt forms[6-8,10,11] for the areas of curative and preventive health care[12,14,30,35] since ancient times.[2,11,34-37]

Owing to its above mentioned properties and tremendous application potential in a wide variety of industrial fields, Ag has been considered as one of the major functionalizing agents[30,31] for the ever-growing polymer nanocomposites market.[8,29] Also, the recent market forecasts indicate that the global utilization of high value-added[37] composites made up of with Ag has already exceeded million ton levels (>4) by the year 2011, with a promising annual growth rate of 24% and an expected demand worth of ~$1 billion.[8,29,30] To properly address this increasing demand researchers from both academia and industry have agreed upon the implementation of "green" methods to synthesize Ag in its NP form.[8] These methods, which can be easily adapted to modern advancements in nanotechnology, aim to progressively relieve the cost pressure,[3] increase the efficiency of the as-synthesized material[3] and more importantly maximize the use of environmentally benign solvents and nontoxic chemicals for the synthesis.[8]

Thus, as an effort to minimize the impact of Ag on the environment[14] and to act accordingly with the above-mentioned goals of the green synthesis methods, Ag has been commonly used in its NP form while getting homogenously dispersed/embedded inside polymeric matrices to form functionally advanced nanocomposites. Especially their tunable morphologies and inherent long chains with relevant functional groups, which would act as targeted reactive sites and allow the controllable immobilization of Ag NPs, are considered as the main reasons for choosing polymers as hosts.[8,30]

Another reason for the need of these composites synthesis is closely related with the toxicity of Ag^+ ions released from Ag NPs. Based on the ongoing debates for a long while many researchers believe that nano Ag and its cations are relatively safe for mammalian, plant and other multi-celled organisms' cells and their beneficial enzymes but it is hard to withdraw a commonly accepted conclusion from this topic.[14,30] So, the synthesis of polymeric composites impregnated with Ag NPs has been offered as an advantageous solution to tackle this potential drawback[14] by hindering the release of Ag^+ ions to these cells' environment for a longer time[2] and restraining their direct uptake of Ag NPs.[30] In this manner, a great deal of research efforts have been spent on various studies, e.g. Jeon *et al.*, Sotiriou *et al.* and Gu *et al.* prepared the long-time chemically durable silica/Ag nanocomposites,[2,14,33] Dowling *et al.* used polyurethane,[34] Shi *et al.* used poly(tetrafluoroethylene),[36] Kong *et al.* used poly(methyl methacrylate)[35] and Xue *et al.* used super hydrophobic cellulose fibers[37] where Nair *et al.* preferred to use methoxybenzyl chloride[29] as a host polymer to obtain their composites in gram scale.

Among CPs family, PANI has been the most extensively studied one with respect to its many advantages such as easy and straightforward preparation,[38-41] low cost and high polymerization yield,[40] unique electrochemical and optical properties,[32,40] relatively high conductivity,[38-41] long-term chemical, thermal and environmental stability,[32,38-42] good processability[42] and most importantly its reversible (acid/base) doping/dedoping pathways identified with its structural chain nitrogen.[42] Thus, all these factors have spurred the use of PANI to fabricate its above mentioned nanocomposites with Ag through different polymerization reactions, which were majorly carried out either in acidic (acetic,[43] nitric,[40,41,44,45] formic,[46]

hydrochloric,[42] methane sulfonic[47] and sulfuric[32]), ionic liquid,[38] organic solvent[48] or aqueous[39,49] media.

As for the synthesis, the in-situ redox reaction between two non-conducting chemicals,[43,46] namely aniline and silver nitrate ($AgNO_3$), has been widely used as an efficient method to obtain nanocomposites made up of highly conducting PANI and Ag NPs[45-47] in the simplest manner and with syncretistic advantages.[40,43] The key to success for such reactions is "building substantial binding between nanocomposite compounds via their simultaneous formation". However, this opportunity remains as the biggest challenge of the in-situ method, since compounds' size and morphology must be handled appropriately during the synthesis reaction.

Throughout the last decade nanostructured PANI, with different morphologies from 0-D nanoparticles to 3-D sea urchin-like nanospheres, has been copiously synthesized. Compared to all others 1-D nanostructured PANI, i.e. nanotubes (NTs)[39,45] and NFs,[42,49-53] has attracted intense attention due to their distinctive advantages for antibacterial applications. NTs have been observed to easily penetrate the bacteria cell wall like a syringe; form artificial pores and cause cell lysis,[23,24] whereas NFs offer a vast, highly porous scaffold which is more favorable for both the expedited immobilization of Ag NPs and for more bacteria cells attachment.[22,42] Upon further consideration of the fact about their synergistic and complimentary behavior to each other,[3,9,16,20] in terms of antibacterial property, PANI NF/Ag NP composites are expected to exhibit superior performance than those of their sole components through a host/guest interaction without any compromise.

Motivation of the current study was to develop a simple, efficient, affordable and an environmentally friendly method for the synthesis of PANI/Ag nanocomposites as advanced

antibacterial agents. To do that, $AgNO_3$ was used as the oxidative and doping agent for aniline to get polymerized through a one-step redox reaction that took place in aqueous medium at ambient temperature. PANI NFs were generated under the guidance of nanofibrous V_2O_5 seeding agents, which were also contributing the reaction as an auxiliary oxidative agent, whilst Ag NPs were simultaneously formed and immobilized within 1-D NFs matrix after getting reduced by them. Here, D.I. water was specifically selected as a "green" solvent in favor of both NF morphology formation and previously mentioned goals of the green synthesis methods, to obtain intimately connected and uniform PANI/Ag nanocomposites.

2.2 Experimental section

2.2.1 Materials and methods

Silver nitrate ($AgNO_3$), aniline and ammonium peroxydisulfate (APS) were all purchased from Alfa Aesar and used as-received. Other reagents including potassium nitrate (KNO_3) and acetone (J.T. Baker) were of analytical grade and used without further purification. V_2O_5 sol-gel NF was prepared based on a previously reported method (Bailey *et al.*, *J. Mater. Res.* 1992, 7, 2530) by using ammonium metavanadate (NH_4VO_3, Acros Organics) and Dowex Marathon (H) ion exchange resin (Sigma Aldrich) in D.I. water. Bacteria cultures of *Staphylococcus aureus* (ATCC 6538) and *Escherichia coli* O157:H7 (ATCC 43895) were purchased from American Type Culture Collection (Rockville, MD), and Trypticase soy agar was obtained from Difco Laboratories (Detroit, MI).

2.2.2 One-step synthesis of PANI NF/Ag NP composite networks

In a typical experiment, 1 mL of V_2O_5 sol-gel NF was gently introduced into 50 mL pre-stabilized D.I. water under magnetic stirring and changed its colour to orange. After 10 min.

magnetic stirring at ambient conditions, 0.1 mL of aniline monomer was added into this medium. Upon the preliminary oxidative interactions between monomers and V_2O_5, starting from the first half of the following 10 min. stirring, well-dispersed fibrous structures were being formed while changing the medium colour to greenish yellow. Eventually, to obtain differently concentrated solutions of $AgNO_3$ (from 0.005 M up to 0.1 M) and to initiate the oxidative polymerization reactions, required amounts of metal salt was weighed and added into each system (Figure 18).

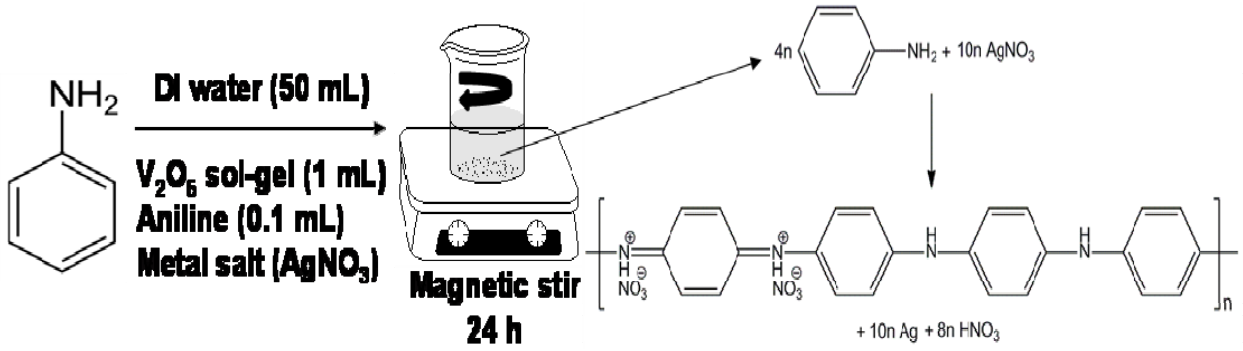

Figure 18. Illustration of the one-step PANI/Ag nanocomposite synthesis

Since the synthesis reaction was conducted in aqueous medium and low concentrated $AgNO_3$ solutions ($\leq$ 0.02 M) were a little lack of oxidative potential to polymerize all aniline monomers in the reaction medium; solution colours became greyish transparent instead of dark, indicating the partial formation/dispersion of fibrous PANI precipitates. Thus, to compensate this oxidative potential difference, catalytic amount (0.057 g) of APS was finally added into these systems after 10 min. extra stirring and this caused the expected darkening in reaction media colours.

A further reaction time of 24 h was given to all systems in order to obtain PANI NFs decorated with Ag NPs. At the end, resulting precipitates were suction filtered while getting

washed with copious amounts of DI water and acetone, respectively. The damp precipitates were allowed to dry overnight in a vacuum oven at 80 °C. The yield of nanocomposite powders from different systems was ranging between 45-90 mg, since the Ag NP loading was determined by initial $AgNO_3$ concentration.[54]

2.2.3 Open circuit potential measurement of the PANI/Ag synthesis reactions

The OCP measurements were conducted on a CHI-601 D electrochemical workstation equipped with a conventional three-electrode cell system. The three-electrodes, composed of platinum (Pt) gauze as the working (WE), Pt wire as the counter (CE) and Ag/AgCl as the reference (RE), were immersed into the reaction medium. Before taking the measurements and adding reactants, 0.01 M of KNO_3 was added into 50 mL D.I. water, under magnetic stirring, in order to decay and stabilize the reaction potential at a steady state that took at most 20 min. The open circuit condition was applied to the electrode cell system, while no current was passing through, and the potential difference between the WE and RE was monitored continuously. A standard synthesis process (above explained) was performed and its overall potential was monitored simultaneously as a function of time.

2.2.4 Structural characterization of the as-obtained PANI/Ag nanocomposites

Different characterization techniques were used systematically to identify PANI/Ag nanocomposite networks. The overall morphology and composition of PANI/Ag were analysed by JEOL JSM-7000F scanning electron microscope (SEM) equipped with an energy dispersive X-ray (EDX) detector. In-depth morphological analysis of PANI/Ag and crystalline nature determination of the Ag NPs were performed on a JEOL 2100F high resolution transmission electron microscope (HR-TEM) operated at 200 kV and on a selected area electron diffractometer (SAED), respectively. The UV-Visible light absorbance spectrum of PANI/Ag

were obtained from a SHIMADZU UV-2450 spectrophotometer. The identification of the characteristic functional groups in PANI/Ag was done via Fourier Transform Infrared (FTIR) analysis, conducted on a Thermo Nicolet 6700 instrument. The thermal stability, solid residual and Ag content of each PANI/Ag were all determined by thermal gravimetric analysis (TGA) performed on a TA Q2000 system. The optical nature of crystalline Ag nanoparticles formed during the synthesis reactions was explained by X-Ray diffractometry (XRD) analysis, which was performed on a Rigaku powder X-Ray diffractometer.

2.2.5 Antibacterial efficacy tests with PANI/Ag nanocomposites

The antibacterial efficacy of PANI/Ag was evaluated against both Gram-positive *Staphylococcus aureus,* and Gram-negative *Escherichia coli* O157:H7 through the dynamic flask shaking and sandwich tests.

2.2.5.1 Dynamic flask shaking test

In a typical procedure, 10 mg PANI/Ag was placed in sterilized 3 mL test tubes, and then inoculated with 1 mL of a known concentration of bacteria suspension. Test tubes were rotated using a Mini LabRoller Rotator for specified contact times of 15, 30, 60 and 120 min., and then the bacterial solutions were serially diluted using 100 mM phosphate buffer solution (PBS) at pH 7 and placed on Trypticase soy agar plates. The viable bacteria colonies were enumerated after incubation at 37 °C for 24 h. The same procedure, without the presence of PANI/Ag, was followed as the control.

2.2.5.2 Sandwich test

1"x1" filter paper swatches with ~15.5 wt% PANI/Ag sample on them were used for this test. Briefly, bacteria were suspended in 100 mM PBS (pH 7) solution to obtain their certain concentrated suspensions. Next, 25 μL of this suspension was placed on a swatch, and then an

identical swatch was placed on top of it. In order to ensure adequate contact with bacteria, a sterile weight was applied on top of this sandwich. After 15, 30, 60 and 120 min contact times, the whole sandwich was placed in tornado tubes containing 5 mL of 0.02 N sodium thiosulfate ($Na_2S_2O_3$) solution, and vortexed for 2 min. so that viable bacteria would be transferred from swatch surfaces to the solution. Eventually, serial dilutions were prepared using 100 mM PBS at pH 7, and placed on Trypticase soy agar plates. After incubation at 37 °C for 24 h, the viable bacteria were counted. The same procedure was followed for the uncoated filter papers, which served as control samples.

2.3 Results and discussion

2.3.1 OCP measurement results of the one-step nanocomposite synthesis reactions

The illustration of the one-step synthesis of PANI/Ag nanocomposites is shown in Figure 18. A plausible formation mechanism is also proposed along with the results obtained from the OCP measurements in Figure 19.

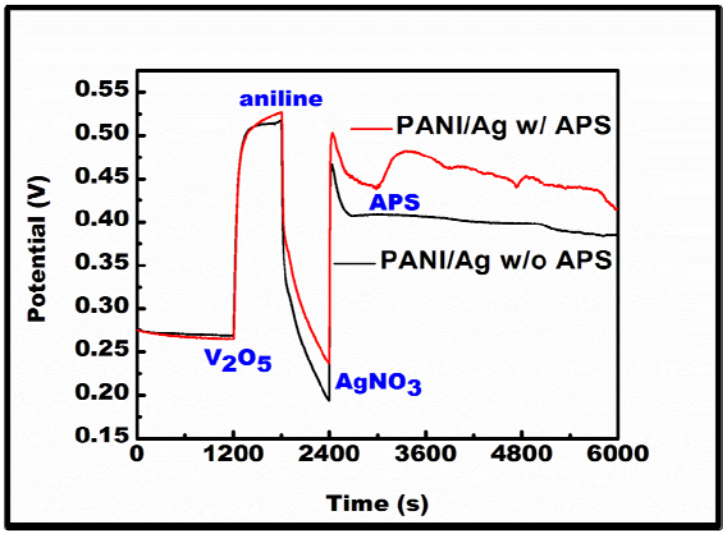

Figure 19. OCP patterns of the aqueous PANI/Ag synthesis reactions with and without APS

The in-situ monitoring of oxidative potential *vs.* time profiles for two nanocomposite synthesis procedures, with and without APS, clearly revealed the dual role of V_2O_5 NFs both as seeding agents and as auxiliary oxidative agent. In contrast to the above mentioned common synthesis reactions conducted in acidic media, the current "green" synthesis was carried out in D.I. water since it is an environmentally friendly, neutral solvent favorable for nanofibrous PANI synthesis.[45] However, the oxidative potential of just $AgNO_3$ was not enough to initiate an aqueous polymerization reaction at room temperature in timely manner.[38] Thus, the addition of catalytic amount of V_2O_5 NF seeds in the reaction media; (i) enhanced the overall oxidative potentials of both systems beyond 0.5 V, (ii) coordinately helped $AgNO_3$ to exceed the oxidation threshold of aniline via pre-oxidizing monomers at its surface, and (iii) provided rapid reaction kinetics for the synthesis of PANI/Ag (less than two hours the reaction potential reached steady-state). Meanwhile, the as-synthesized PANI exhibited bulk NF morphology due to the seeding effect of V_2O_5 NFs, through which, their morphology was duplicated by monomers and nanofibrous PANI oligomers were formed as reactive seeds which would further promote bulk NFs formation.[54]

2.3.2 Structural characterization results of the PANI/Ag nanocomposites

Morphological features of the as-synthesized PANI/Ag nanocomposites were verified by SEM and HR-TEM characterizations. Figure 20A shows the homogenously embedded/dispersed Ag NP clusters, with 400-450 nm average diameters, in 1-D PANI NF matrix. The same SEM image also shows the highly dense, straight and microns long PANI NF network with narrow pores in it. The bright, prominent spots observed in this image, with ~500 nm average diameters, indicate the embedded Ag NP clusters with high electron densities inside PANI NF matrix. The EDX analysis of these spots and the more fibrous phase (Figure 21) proved that they were

composed of elemental Ag and PANI NFs, respectively (Table 2). Like in other noble metal NP systems, Ag NPs were also tending to form clusters during the synthesis reactions due to their high surface energies, but they still kept their "particle" shapes on those clusters simply because of their electrochemical interactions with PANI NFs.

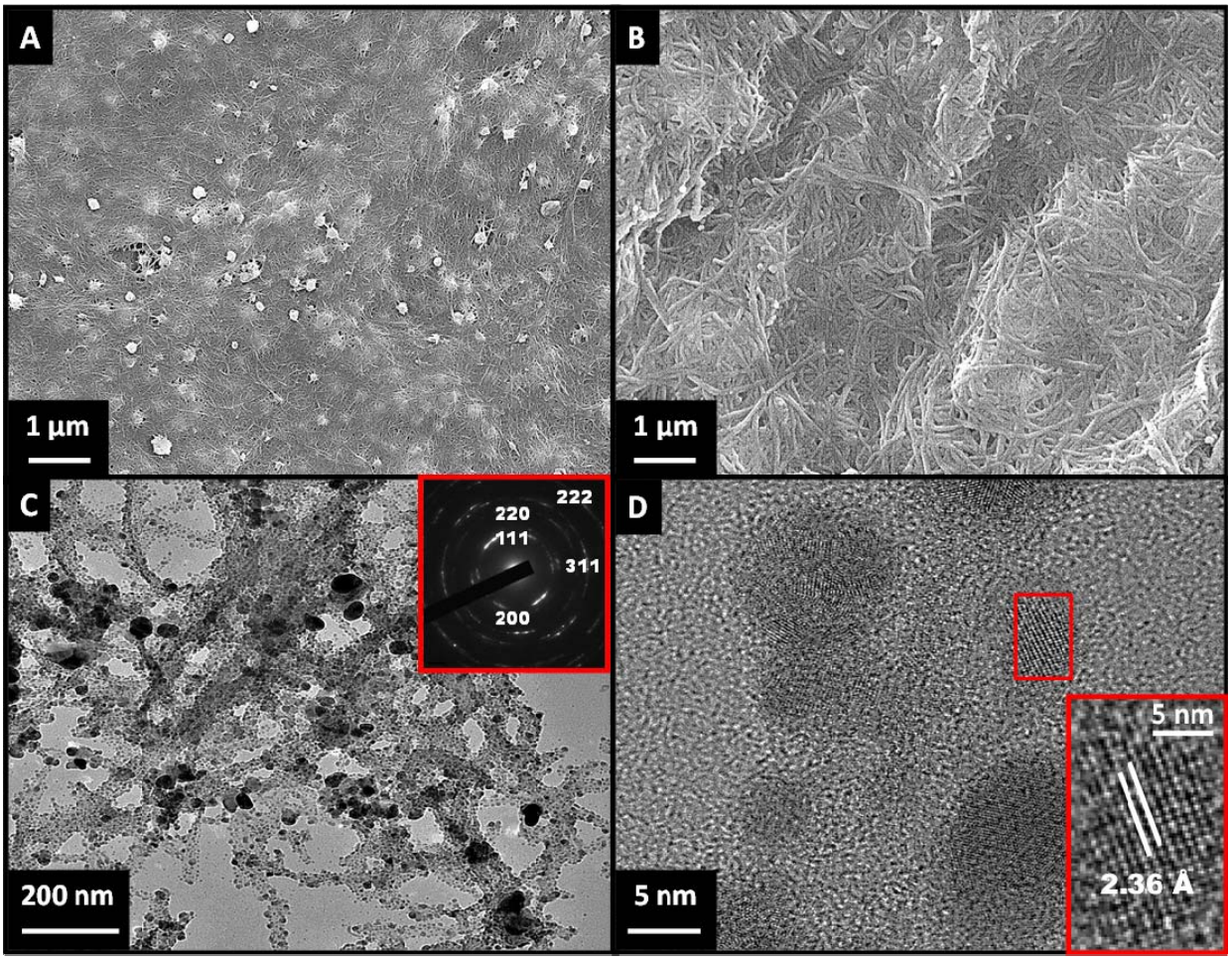

Figure 20. SEM images of; (A) PANI/Ag nanocomposite showing homogenously dispersed/embedded Ag NPs within PANI NF matrix, (B) zoomed-in fibrous PANI phase, (C) TEM image of PANI/Ag nanocomposite (Inset is the SAED pattern of Ag NPs), and (D) HR-TEM image of individual Ag NPs embedded into PANI NF matrix (Inset shows the zoomed-in view of crystal lattice spacing in a single Ag NP)

Furthermore, similarly formed NP clusters were expected to exhibit distinctive size-dependent properties owing to their NPs' narrow particle size distribution (PSD) and facet compositions. On the other hand, PANI NF network was composed of 30-40 nm average diameter fibers and had very tight nanopores formed among its NF interspaces (Figure 20B).

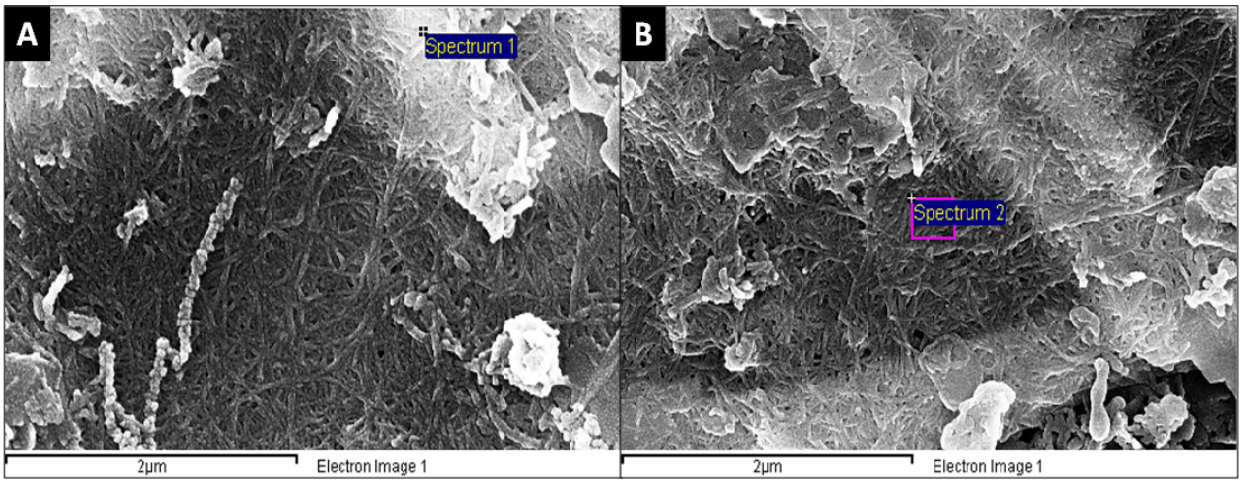

Figure 21. SEM images of; (A) a bright spot indicating embedded Ag NP presence in PANI NF matrix, (B) nanofibrous PANI phase decorated with Ag NPs, respectively.

Table 2. Summary of the EDX analysis results from Figure 21

	C	**Ag**	**Au**	**Total**
Bright spot (Atomic %)	-	92.17	7.83	100
Bright spot (Weight %)	-	86.57	13.43	100
Fibrous phase (Atomic %)	69.64	30.36	-	100
Fibrous phase (Weight %)	20.34	79.66	-	100

Further characterization of PANI/Ag by HR-TEM provided more detailed information about its morphological properties. Similarly to the SEM results, Ag NPs with average diameters from 5-65 nm could be seen as homogenously decorating the PANI NFs web-like network composed of ~35 nm thick fibers (Figure 20C). The SAED pattern (Figure 20C inset) of Ag NPs indicate that they were perfect crystals, which were composed of small oxidized NPs with a PSD majorly (> 75%) less than 10 nm (Figure 22). Additionally, 0.236 nm average lattice fringe spacing of individual Ag NPs in Figure 20D/inset was in good accordance with the previous literature,[29] indicating the presence of discrete (111) crystalline domains inside them. Here, the discrepancy between the sizes of Ag NPs in SEM and HR-TEM images could be attributed to the sonication process that was applied for sample preparation purposes. The primary effects and advantages of these obvious morphological features on the antibacterial property of PANI/Ag would be explained in details along the following sections.

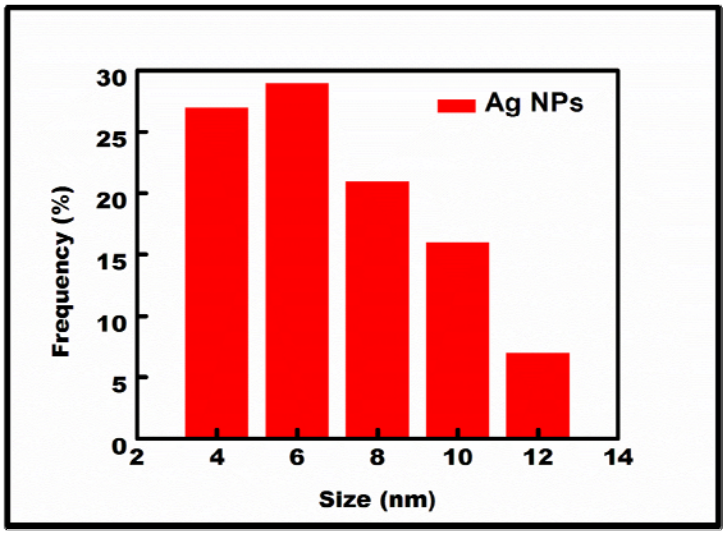

Figure 22. PSD analysis graphic of Ag NPs decorating the PANI NF network

After confirming the morphological features of PANI/Ag by using SEM and TEM instruments, their further characterizations including the thermal, spectroscopic, crystallographic and optical analyses were completed by using relevant techniques. Firstly, PANI NF and PANI/Ag nanocomposites were heated from room temperature up to 800 ºC (at a heating rate of 10 ºC/min, in O_2 atmosphere) to determine the solid residue amount and the thermal stability of these samples. Figure 23A and its inset show the TGA graphics obtained from these heating processes, according to which, there were three main temperature regions that the samples went through major weight losses. The first major weight loss, observed up to 100 ºC, was corresponding to the loss of water molecules/moisture that existed in the samples.[41,44] The secondary weight loss, observed up to 275 ºC, could be attributed to the volatilization and loss of nitrate (NO_3^-) dopants,[38,41,44] low molecular weight oligomers and unreacted substances that were attached to the primary PANI chains.[3,9,20] The third major weight loss, observed between 300-450 ºC, took place due to the oxidative decomposition of primary PANI NF backbone in each nanocomposite sample.[20,38] The extra weight loss occurred around 550 ºC was probably due to the decomposition of complex structures that were formed at the initial stages of the synthesis reactions at the interface of PANI NFs and Ag NPs.[54] The TGA results could be summarized as; (i) compared to bare PANI NFs, both the thermal stability and solid residue content of PANI/Ag samples were increased with the initial $AgNO_3$ concentration,[3] (ii) Ag NP loading in PANI/Ag samples was found to be around 57-77 wt%[38,44] and (iii) presence of PANI oligomers and polymeric PANI with different decomposition temperatures were observed in all samples due to the reasons listed in the nanocomposite synthesis section.[41,44] Lastly, the complexation process took place between Ag NPs and amine/imine groups in PANI NFs reduced the as-formed PANI

chains' mobility and caused a suppressive effect on chain transfer reactions, which positively contributed the nanocomposites' thermal properties.[42]

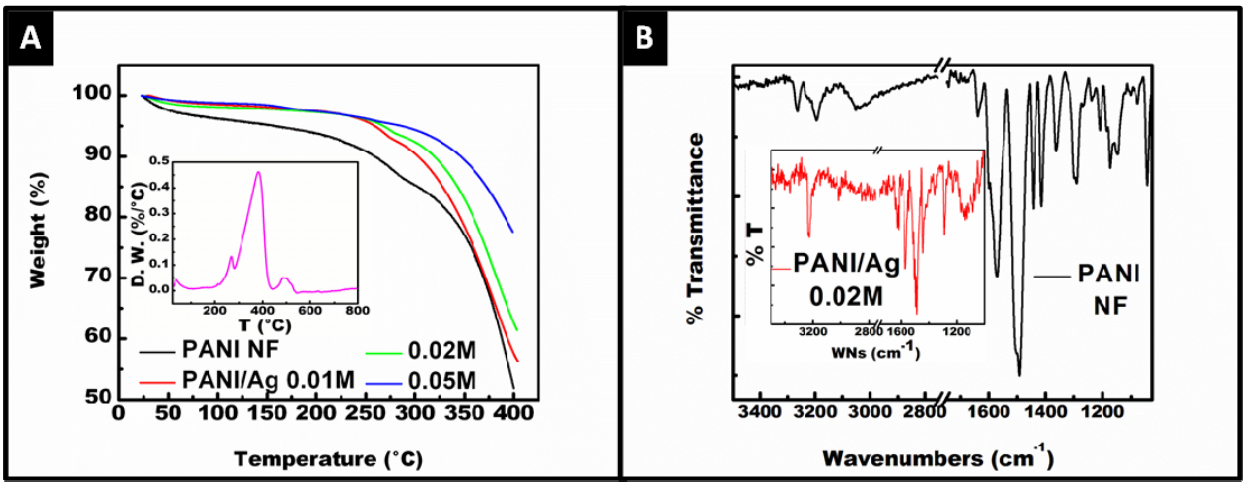

Figure 23. (A) TGA thermograms (Inset: derived weight loss graphic) and (B) FT-IR spectra of PANI NF and PANI/Ag (Inset: 0.02 M system's sample) nanocomposite samples

FT-IR was used to investigate both pristine PANI NFs and stock PANI/Ag nanocomposite (Figure 23B). This characterization was applied to gain more insight about the formation of these nanostructures[39] and to confirm the presence of doped PANI by locating its functional groups' corresponding peaks and comparing their intensities.[42] Based on PANI NF's spectrum, the two distinct peaks located before and after 3200 cm^{-1} could be assigned to the asymmetric and symmetric stretching modes of an aromatic amine (N-H) belong to a $–NH_2$ group, respectively.[16,20,41] The following broad peak around 3050 cm^{-1} was corresponding to a C-H stretching vibration.[9,20,38] A smaller peak, appeared around 1635 cm^{-1}, was characteristic of C=C stretching at quinoid (Q) and benzoid (B) emeraldine state PANI rings, respectively.[42] This peak was also assigned to N-H scissoring vibration of an aromatic amine.[47] Following two sharp

peaks around 1570 cm^{-1} and 1495 cm^{-1} were corresponding to the stretching modes of N-Q-N and N-B-N groups of protonated PANI, respectively.[38-42,46,47] The two identical but less sharp peaks located at 1444 cm^{-1} and 1415 cm^{-1} were related with the presence of oxidized and protonated aniline oligomers, respectively.[44,46] After these peaks, the next one around 1360 cm^{-1} was assigned to stretching vibrations of an aromatic C-N group.[9,20] The following sharper peak around 1290 cm^{-1} indicating the stretching of C-N group with secondary aromatic amine conjugation.[32,39,40] Next peak at 1200 cm^{-1} with a little hump around 1240 cm^{-1} was either referring to the quinoic units in protonated PANI NF[16,41] or to the stretching vibration of $C\text{-}N^{(+\cdot)}$ group in polaron structure.[40,47] The following larger peak with two ends at 1170 cm^{-1} and 1140 cm^{-1} was characteristic of $-N{=}Q\text{-}N^{+}\text{-}B-$ group in protonated PANI and stretching mode of C-N or in plane C-H bonds, respectively.[38-40] Lastly, the peak around 1040 cm^{-1} corresponds to the stretching vibrations of SO_3H^- group in APS doped PANI NF.[20,38,47] The majority of the above listed characteristic PANI peaks, including the ones at 3200 cm^{-1}, 1635 cm^{-1}, 1570 cm^{-1}, 1495 cm^{-1} 1444 cm^{-1} and 1290 cm^{-1}, could be also observed in PANI/Ag spectrum with some intensity loss and overlapping features (Figure 23B inset). Most importantly, the peak around 1385 cm^{-1} proved the nitrate ($-NO_3$) counter ions presence in nanocomposites,[20,44,46-48] which were inserted in PANI NF backbones during the charge neutralization/doping process.

Crystalline nature of the as-obtained nanostructures was investigated by XRD analysis. Figure 24A shows the registered diffractograms of PANI NFs and PANI/Ag nanocomposites from 0.01 M and 0.02 M systems, respectively. One broad and one sharper band on PANI NF's diffractogram, centered at $2\theta = 20^{o}$,[3,9,16,20] and 25^{o},[32,38,39,42] were ascribed to the parallel and perpendicular periodicity of amorphous PANI chains. Another distinctive band observed around $2\theta = 45^{o}$, was indicating the presence of local, partially crystalline PANI chains in NFs.[49,50,55]

These characteristic bands were broadened and diminished on PANI/Ag nanocomposite diffractograms due to the presence of highly crystalline Ag NPs in their structure. Here, the first two sharp and the latter three small peaks, located respectively at 2θ = 38º, 44º, 64º, 77º and 82º, were representing the Bragg's reflections from (111), (200), (220), (311) and (222) planes of Ag NPs.[3,9,32,40-42,48] These results were in good accordance with the previously mentioned SAED pattern (Figure 20C inset), HR-TEM image (Figure 20D inset) and the standard literature data, e.g. JCPDS No. 4-783,[20,33,37-39,49] which are strongly indicating the existence of face-centered cubic (fcc) Ag NPs with dominant (111) lattice planes, immobilized in PANI NF matrix. Additionally, the effect of initial $AgNO_3$ concentration used for the nanocomposite synthesis on metal NPs' crystalline peak intensities could be obviously seen from these diffractograms, as well.

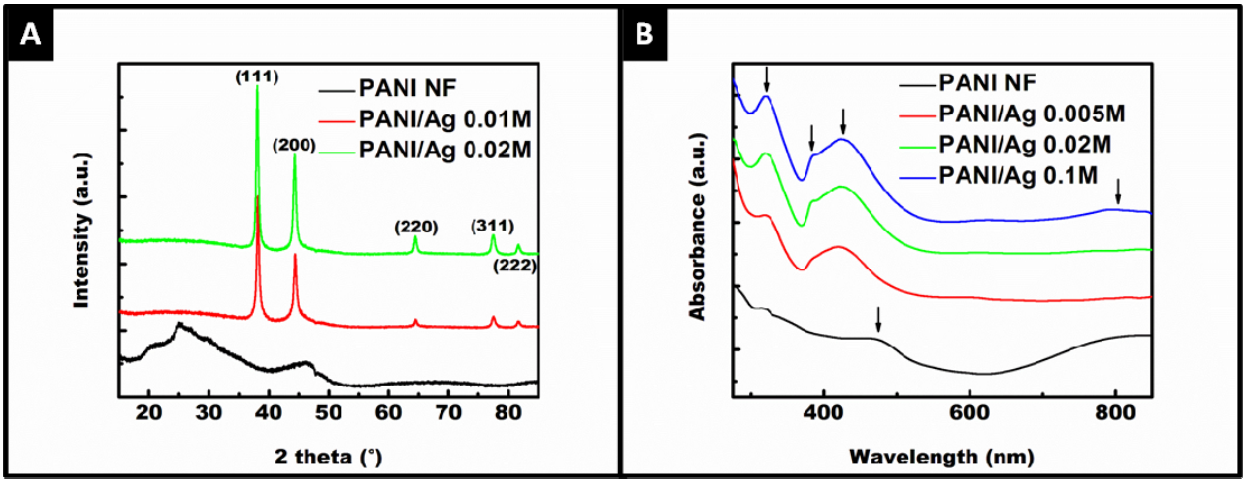

Figure 24. (A) XRD diffractograms and (B) UV-Vis spectra of PANI NF and different PANI/Ag nanocomposites

Lastly, the optical properties of PANI NFs and three different PANI/Ag nanocomposites from 0.005 M, 0.02 M and 0.1 M concentrated systems were characterized by UV-Visible spectroscopy. From the PANI NF spectrum in Figure 24B, a tiny absorption peak located around 300-350 nm could be observed via indicating the π-π* transition of benzoid rings in doped PANI chains.[9,16,41-44] The following broad shoulder at the same spectrum, located around 450-500 nm, was assigned to the polaron-π* transition of localized band and indicating protonated/half oxidized PANI structure for the NFs.[38,50,55] The last peak with a very broad free carrier tail, located around 800 nm, was ascribed to the π-polaron transition of emeraldine base PANI backbone.[3,20,32,39] Moreover, all three PANI/Ag nanocomposites' spectra in Figure 24B were clearly exhibiting the above mentioned characteristic absorption peaks of PANI, especially at higher concentration of $AgNO_3$. However, there was a high possibility of shifting in those peaks towards to the red region due to the oxidative interactions between PANI and $AgNO_3$ which took place along the nanocomposite synthesis.[9,38,42] During the in-situ polymerization reaction, $AgNO_3$ was reduced by nitrogen at amine groups via transforming them into imines.[20] Also, the overlapping feature between the surface plasmon resonance (SPR) peak of embedded Ag NPs and polaron band of PANI could be clearly observed from each PANI/Ag nanocomposite's spectrum.[3,32,39] The SPR peak appeared as a tiny shoulder on the polaron PANI band around 400 nm with an increasing intensity proportional to the initial $AgNO_3$ concentration, just like the other characteristic PANI peaks on these spectra.[2,46,48]

2.3.3 Antibacterial efficacy tests results of the PANI/Ag nanocomposites

Upon completion of the in-depth characterizations of PANI NFs and PANI/Ag nanocomposites, the success of the as-proposed one-step, oxidative seeding agent-assisted polymerization reaction was confirmed. After that, antibacterial efficacies of these

nanostructures against Gram-positive and Gram-negative bacteria strains were further evaluated by dynamic flask shaking and sandwich tests.

2.3.3.1 Dynamic flask shaking test results

The results obtained from two different dynamic flask shaking tests were summarized in Figure 25 and Table 3.

Table 3. Summary of the antibacterial efficacy results from dynamic flask shaking tests

Sample	**Contact time (min)**	**Viable bacteria colony reduction (log)**	
		S. aureus	*E. coli* O157:H7
Filter paper	120	0.04	0.01
PANI NF	120	0.16	0.05
PANI/Ag 0.02 M	15	2.58	0.94
	30	2.48	3.61
	45	2.68	6.34
	60	2.76	6.34
	120	2.84	6.34
PANI/Ag 0.01 M	60	2.50	4.51
PANI/Ag 0.02 M	60	2.76	6.34
PANI/Ag 0.05 M	60	6.16	6.34
PANI/Ag 0.10 M	60	6.16	6.34

It can be seen that the control (empty filter paper) sample did not exhibit any obvious reduction in viable bacteria colonies even for the longest contact time, but since PANI is a

known biocide,[17-19] the other control sample with just PANI NFs caused a very limited reduction (Table 3). On the other hand, introduction of Ag NPs into PANI NFs significantly enhanced the antibacterial efficacy of nanocomposites for both types of bacteria. Thus, PANI/Ag nanocomposites were evaluated in two different ways to indicate the effect of Ag NPs presence on the antibacterial property. Firstly, stock PANI/Ag nanocomposite sample from 0.02 M concentrated system was used against both bacteria strains during different contact times, i.e. 15, 30, 45, 60, 120 min., in order to reveal the kinetic reduction effect. And to analyze the effect of Ag concentration, in the second experiment, different PANI/Ag nanocomposites from 0.01 M, 0.02 M, 0.05 M and 0.1 M concentrated systems were used against both bacteria strains during constant contact time of 60 min.

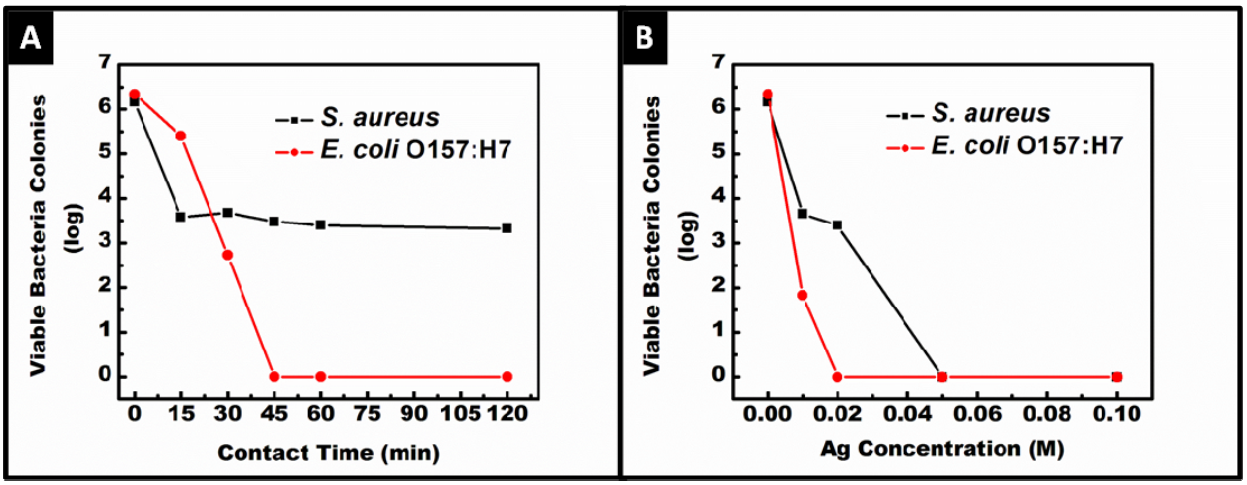

Figure 25. Antibacterial efficacy test results obtained from dynamic flask shaking (A) with PANI/Ag 0.02 M nanocomposite for different contact times and (B) with PANI/Ag nanocomposites from 0.01 M, 0.02 M, 0.05 M and 0.1 M systems for 60 min. contact time

Based on the results shown in Figure 25A, longer contact time increased the reduction of viable bacteria colonies. Here, the reduction in *E. coli* was more obvious than that of *S. aureus*. Also, as expected, higher Ag concentration in nanocomposite samples caused more inactivation in both strains (Figure 25B). That was a clear indication for Ag NPs to be the predominant biocide in nanocomposite structures. Moreover, the PANI/Ag nanocomposite from 0.05 M system succeeded in complete inactivation of both bacteria strains within 60 min. contact time. Generally, for all different Ag concentrations, PANI/Ag nanocomposite seemed to be more effective on Gram-negative bacteria than it was on Gram-positive. For instance, the stock PANI/Ag nanocomposite was able to completely inactivate all *E. coli* bacteria within 45 min. contact time, whereas it could only cause ~2.7 log reductions on *S. aureus*. As previously observed in various studies, this result was clearly indicating the difference in resistance against Ag for these bacteria strains that originates from their peptidoglycan layouts. Thus, having a thicker peptidoglycan layer around its cell provides more protection to *S. aureus* and effectively prevented the penetration of Ag NPs through its cell wall.[3,11,13,24,56]

2.3.3.2 Sandwich test results

More reliable antibacterial efficacy simulations on surfaces were carried out through sandwich tests by using the above mentioned samples-coated filter papers. Since PANI/Ag 0.02 M nanocomposite sample provided sufficient inactivation for the dynamic flask shaking test, corresponding nanocomposite sample coated filter paper swatches were used for this test along with just PANI NF coated ones and the uncoated filter papers, serving as controls. The as-obtained results from these tests were shown in both Figure 26 and Table 4, respectively. As can be seen in Table 4, empty filter paper provided about 0.55 and 0.3 log reductions against *S.*

aureus and *E. coli*, respectively. This reduction was either caused by the adhesion and/or the physical entrapment of bacteria cells within the fibrous matrix of the filter paper.

Table 4. Summary of the antibacterial efficacy results from sandwich tests

Sample	**Contact time (min)**	**Viable bacteria colony reduction (log)**	
		S. aureus	*E. coli* O157:H7
Filter paper	120	0.53	0.28
PANI NF	120	1.85	2.39
PANI/Ag 0.02 M	15	1.54	6.50
	30	1.85	6.50
	60	2.16	6.50
	120	2.52	6.50

On the other hand, due to its above mentioned biocide property, pristine PANI NF coated swatches provided limited inactivation of 1.85 and ~2.4 log reductions on each bacteria strain within 120 min. contact time, respectively. Similarly to the dynamic flask shaking test results, PANI/Ag 0.02 M nanocomposite containing sandwiches provided powerful antibacterial performance via complete inactivation of the Gram-negative bacteria cells and 1.54 log reduction on the viable Gram-positive colonies, within 15 min. contact time. This result was most probably related with the increased exposure of *E. coli* cells to PANI/Ag nanocomposite in sandwich form. However, increasing contact times did not significantly improve the efficacies against *S. aureus* cells. Although it was not presented here, based on the dynamic flask shaking test results

it was anticipated that by using PANI/Ag nanocomposites from higher concentrated systems, better efficacies against Gram-positive bacteria could be obtained.

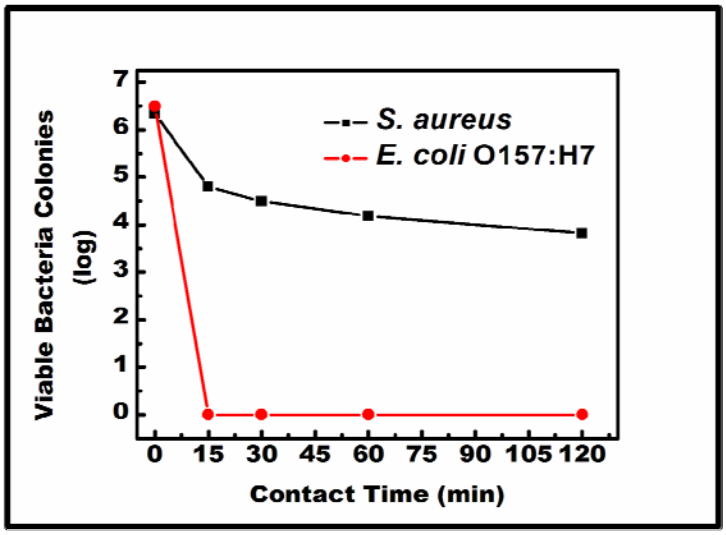

Figure 26. Antibacterial efficacy test results obtained from sandwich tests with PANI/Ag 0.02 M nanocomposites for 15, 30, 60 and 120 min. contact times

2.4 Antibacterial property working mechanisms of PANI NFs and PANI/Ag nanocomposites

The broad spectrum antibacterial performances of PANI NF and different PANI/Ag nanocomposite samples were evaluated in details via dynamic flask shaking and sandwich tests. It was proven that both samples were able to kill and/or inhibit the growth of medically hazardous Gram-positive and Gram-negative bacteria strains.[3,16-20] Based on these test results, a plausible working mechanism about the antibacterial properties of PANI NFs and PANI/Ag nanocomposites is proposed and strongly supported with the information from the previous literature as follows.

Compared to PANI/Ag nanocomposites, the pristine PANI NFs exhibited a limited antibacterial performance in both tests against *E. coli* and *S. aureus*, which was mainly related with its chemical nature.[19] Since they were synthesized in neutral medium, i.e. D.I. water, PANI NFs were lack of acidic dopant molecules on their primary backbone chains, which are the main compounds that their antibacterial property depends on.[19] Other than these molecules, different polarity charge transfer process, which took place when PANI NFs and bacteria cells electrostatically adhered to each other could be another important factor providing antibacterial property for PANI NFs.[18,19] Last but not least, PANI NFs' higher antibacterial performance against *E. coli* could be ascribed to their multi-layered Gram-negative cell walls with low osmotic pressure, which facilitated their physical interactions.[3] Additionally, the surface hydrophilicity, polymeric chain length, low molecular weight and inherent amino groups presence could be listed as the other important factors[16] for PANI that (i) increased the overall permeability of bacteria cell membranes and (ii) exerted repressive effect on damage-responsive genes, which are primarily involved in energy metabolism and transport, cell wall repairment and formation of stress-resistant biofilms, in order to mitigate potential chances of the emergence of bacterial resistance.[16,17]

As for the silver component's antibacterial working mechanism, chances were either related with (i) the size distribution and nature of its NPs or (ii) the release rate of its cations towards the bacteria medium and their possible physicochemical interactions with electron donor biological molecules containing S, O, N or essential metal cations in bacteria cell walls such as Ca^{2+} or Zn^{+}.[6,12-15,30,34] Based on the PSD analysis results, >75% of the Ag NPs in PANI/Ag nanocomposites were found in the size range of 4-8 nm. Along with the previous literature, this data indicates a large amount of Ag^{+} release took place from Ag NPs surface to the bacteria

environment, which would interfere with the metabolic pathways, i.e. ATP production and DNA replication,[30] of bacteria cells and provide the major antibacterial property for PANI/Ag nanocomposites.[13,14,24] Also, the penetration and binding strength of these NPs in bacteria cell membranes were observed to be higher, which is advantageous for their bactericidal effect that is based on chemically interacting with the S and P containing compounds, i.e. DNA or proteins,[1,8] and causing malfunctioning on them.[13] However, the rest ~25% of Ag NPs (up to 12 nm particle size) were also effectively contributing the antibacterial performance of PANI/Ag nanocomposites via getting attached to the bacteria cell membranes and disturbing their in-cell transport or respiratory functions.[8,13,14] In addition, on the readily oxidized and highly reactive (111) facet dominating surfaces of such NPs, large amounts of oxidative stress and reactive oxygen species were formed and they disrupted the lipids, cytoplasm and the DNA of bacteria cells.[1,6,8,13,30] As repeatedly suggested in previous literature; to have a better control on the NP morphology,[6] prolong the release of Ag^+ cations from the NPs,[15,30,34] minimize the toxicity of Ag^+ cations to prevent damaging multi-celled organisms' cells and their beneficial enzymes,[6,14] obtain a synergistic effect on antibacterial property and to optimize its duration,[3,6,9,16] in this study, Ag NPs were homogenously embedded into PANI NFs network.

2.5 Conclusions

Along with the driving force of modern nanotechnology, in order to properly address the demand in constantly expanding nanocomposite market with Ag NPs and to provide a promising solution for the continuously growing threat of the resistant pathogenic microorganisms' emergence, in this study, PANI NF networks with homogenous Ag NP decoration were facilely synthesized in a nanocomposite form. Such nanocomposites were obtained through a one-step,

oxidative seeding template-assisted polymerization reaction, which took place in "green" D.I. water medium at room temperature, without the need of any harsh acids or non-toxic oxidative agents.

According to the strongly supported material characterization results, the as-synthesized nanocomposites were found to exhibit unique chemical and morphological features with substantial integrity between their counterparts, which turned out to be favourable for their final use as powerful antibacterial agents. Besides that, the dynamic flask shaking and sandwich test results provided clear indications for the promising antibacterial property of these nanocomposites against both Gram-positive and Gram-negative bacteria strains. Based on the test results and support from the previous literature, PANI/Ag nanocomposites were found to be more effective on Gram-negative *E. coli* than Gram-positive *S. aureus* due to the difference in their peptidoglycan layouts. Last but not least, the homogenous embedment of Ag NPs into PANI NF networks was proven to have synergistic and complimentary effect on each individual's antibacterial working mechanism, broadened the life span and enriched the dual antibacterial property duration of PANI/Ag nanocomposites.

It is believed that the synthesis of such elaborately combined, hybrid nanocomposites will help to elucidate the insights of their bactericidal working mechanisms and provide more active materials for next generation antibacterial applications.

2.6 References

(1) Morones, J. R.; Elechiguerra, J. L.; Camacho, A.; Holt, K.; Kouri, J. B.; Ramirez, J. T.; Yacaman, M. J. *Nanotechnology* **2005**, *16*, 2346-2353.

(2) Jeon, H. J.; Yi, S. C.; Oh, S. G. *Biomaterials* **2003**, *24*, 4921-4928.

(3) Jia, Q. M.; Shan, S. Y.; Jiang, L. H.; Wang, Y. M.; Li, D. *Journal of Applied Polymer Science* **2012**, *125*, 3560-3566.

(4) Qin, C. Q.; Li, H. R.; Xiao, Q.; Liu, Y.; Zhu, J. C.; Du, Y. M. *Carbohydrate Polymers* **2006**, *63*, 367-374.

(5) Rabea, E. I.; Badawy, M. E. T.; Stevens, C. V.; Smagghe, G.; Steurbaut, W. *Biomacromolecules* **2003**, *4*, 1457-1465.

(6) Simoncic, B.; Tomsic, B. *Textile Research Journal* **2010**, *80*, 1721-1737.

(7) Kim, T. N.; Feng, Q. L.; Kim, J. O.; Wu, J.; Wang, H.; Chen, G. Q.; Cui, F. Z. *Journal of Materials Science-Materials in Medicine* **1998**, *9*, 129-134.

(8) Sharma, V. K.; Yngard, R. A.; Lin, Y. *Advances in Colloid and Interface Science* **2009**, *145*, 83-96.

(9) Boomi, P.; Prabu, H. G.; Mathiyarasu, J. *Colloids and Surfaces B-Biointerfaces* **2013**, *103*, 9-14.

(10) Clement, J. L.; Jarrett, P. S. *Metal Based Drugs* **1994**, *1*, 467-482.

(11) Feng, Q. L.; Wu, J.; Chen, G. Q.; Cui, F. Z.; Kim, T. N.; Kim, J. O. *Journal of Biomedical Materials Research* **2000**, *52*, 662-668.

(12) Schierholz, J. M.; Lucas, L. J.; Rump, A.; Pulverer, G. *Journal of Hospital Infection* **1998**, *40*, 257-262.

(13) Sotiriou, G. A.; Pratsinis, S. E. *Current Opinion in Chemical Engineering* **2011**, *1*, 3-10.

(14) Sotiriou, G. A.; Pratsinis, S. E. *Environmental Science & Technology* **2010**, *44*, 5649-5654.

(15) Xinping, L.; Shengli, L.; Miaotao, Z.; Chuanghong, L. *Rare Metal Materials and Engineering* **2011**, *40*, 0209-0214.

(16) Boomi, P.; Prabu, H. G. *Colloids and Surfaces a-Physicochemical and Engineering Aspects* **2013**, *429*, 51-59.

(17) Gizdavic-Nikolaidis, M. R.; Bennett, J. R.; Swift, S.; Easteal, A. J.; Ambrose, M. *Acta Biomaterialia* **2011**, *7*, 4204-4209.

(18) Seshadri, D. T.; Bhat, N. V. *Indian Journal of Fibre & Textile Research* **2005**, *30*, 204-206.

(19) Shi, N. L.; Guo, X. M.; Jing, H. M.; Gong, J.; Sun, C.; Yang, K. *Journal of Materials Science & Technology* **2006**, *22*, 289-290.

(20) Tamboli, M. S.; Kulkarni, M. V.; Patil, R. H.; Gade, W. N.; Navale, S. C.; Kale, B. B. *Colloids and Surfaces B-Biointerfaces* **2012**, *92*, 35-41.

(21) Chauhan, N. P. S.; Ameta, R.; Ameta, R.; Ameta, S. C. *Journal of Indian Chemical Council* **2010**, *27*, 128-133.

(22) Kong, H.; Jang, J. *Biomacromolecules* **2008**, *9*, 2677-2681.

(23) Kong, H.; Song, J.; Jang, J. *Macromolecular Rapid Communications* **2009**, *30*, 1350-1355.

(24) Park, E.; Kim, H.; Song, J.; Oh, H.; Song, H.; Jang, J. *Macromolecular Research* **2012**, *20*, 1096-1101.

(25) Cerkez, I.; Kocer, H. B.; Worley, S. D.; Broughton, R. M.; Huang, T. S. *Langmuir* **2011**, *27*, 4091-4097.

(26) Kocer, H. B.; Cerkez, I.; Worley, S. D.; Broughton, R. M.; Huang, T. S. *Acs Applied Materials & Interfaces* **2011**, *3*, 2845-2850.

(27) Kocer, H. B.; Cerkez, I.; Worley, S. D.; Broughton, R. M.; Huang, T. S. *Acs Applied Materials & Interfaces* **2011**, *3*, 3189-3194.

(28) Kang, S.; Pinault, M.; Pfefferle, L. D.; Elimelech, M. *Langmuir* **2007**, *23*, 8670-8673.

(29) Nair, A. S.; Binoy, N. P.; Ramakrishna, S.; Kurup, T. R. R.; Chan, L. W.; Goh, C. H.; Islam, M. R.; Utschig, T.; Pradeep, T. *Acs Applied Materials & Interfaces* **2009**, *1*, 2413-2419.

(30) Dallas, P.; Sharma, V. K.; Zboril, R. *Advances in Colloid and Interface Science* **2011**, *166*, 119-135.

(31) Wei, Q. F.; Ye, H.; Hou, D. Y.; Wang, H. B.; Gao, W. D. *Journal of Applied Polymer Science* **2006**, *99*, 2384-2388.

(32) Drury, A.; Chaure, S.; Kroell, M.; Nicolosi, V.; Chaure, N.; Blau, W. J. *Chemistry of Materials* **2007**, *19*, 4252-4258.

(33) Gu, G. X.; Xu, J. X.; Wu, Y. F.; Chen, M.; Wu, L. M. *Journal of Colloid and Interface Science* **2011**, *359*, 327-333.

(34) Dowling, D. P.; Donnelly, K.; McConnell, M. L.; Eloy, R.; Arnaud, M. P. *Thin Solid Films* **2001**, *398*, 602-606.

(35) Kong, H.; Jang, J. *Langmuir* **2008**, *24*, 2051-2056.

(36) Shi, Z. Q.; Zhou, H.; Qing, X. T.; Dai, T. Y.; Lu, Y. *Applied Surface Science* **2012**, *258*, 6359-6365.

(37) Xue, C. H.; Chen, J.; Yin, W.; Jia, S. T.; Ma, J. Z. *Applied Surface Science* **2012**, *258*, 2468-2472.

(38) Correa, C. M.; Faez, R.; Bizeto, M. A.; Camilo, F. F. *Rsc Advances* **2012**, *2*, 3088-3093.

(39) Gao, Y.; Shan, D. C.; Cao, F.; Gong, J.; Li, X.; Ma, H. Y.; Su, Z. M.; Qu, L. Y. *Journal of Physical Chemistry C* **2009**, *113*, 15175-15181.

(40) Reda, S. M.; Al-Ghannam, S. M. *Advances in Materials Physics and Chemistry* **2012**, *2*, 75-81.

(41) Wankhede, Y. B.; Kondawar, S. B.; Thakare, S. R.; More, P. S. *Advanced Materials Letters* **2013**, *4*, 89-93.

(42) Grinou, A.; Bak, H.; Yun, Y. S.; Jin, H. J. *Journal of Dispersion Science and Technology* **2012**, *33*, 750-755.

(43) Blinova, N. V.; Bober, P.; Hromadkova, J.; Trchova, M.; Stejskal, J.; Prokes, J. *Polymer International* **2010**, *59*, 437-446.

(44) Blinova, N. V.; Stejskal, J.; Trchova, M.; Sapurina, I.; Ciric-Marjanovic, G. *Polymer* **2009**, *50*, 50-56.

(45) Stejskal, J.; Prokes, J.; Sapurina, I. *Materials Letters* **2009**, *63*, 709-711.

(46) Bober, P.; Stejskal, J.; Trchova, M.; Hromadkova, J.; Prokes, J. *Reactive & Functional Polymers* **2010**, *70*, 656-662.

(47) Bober, P.; Stejskal, J.; Trchova, M.; Prokes, J. *Polymer* **2011**, *52*, 5947-5952.

(48) Paulraj, P.; Janaki, N.; Sandhya, S.; Pandian, K. *Colloids and Surfaces a-Physicochemical and Engineering Aspects* **2011**, *377*, 28-34.

(49) Gao, L.; Lv, S.; Xing, S. X. *Synthetic Metals* **2012**, *162*, 948-952.

(50) Chiou, N. R.; Epstein, A. J. *Advanced Materials* **2005**, *17*, 1679-+.

(51) Huang, J. X.; Kaner, R. B. *Angewandte Chemie-International Edition* **2004**, *43*, 5817-5821.

(52) Surwade, S. P.; Manohar, N.; Manohar, S. K. *Macromolecules* **2009**, *42*, 1792-1795.

(53) Zhang, X. Y.; Kolla, H. S.; Wang, X. H.; Raja, K.; Manohar, S. K. *Advanced Functional Materials* **2006**, *16*, 1145-1152.

(54) Liu, Z.; Liu, Y.; Zhang, L.; Poyraz, S.; Lu, N.; Kim, M.; Smith, J.; Wang, X. L.; Yu, Y. J.; Zhang, X. Y. *Nanotechnology* **2012**, *23*, 335603-+.

(55) Kan, J. Q.; Zhang, S. L.; Jing, G. L. *Journal of Applied Polymer Science* **2006**, *99*, 1848-1853.

(56) Jung, W. K.; Koo, H. C.; Kim, K. W.; Shin, S.; Kim, S. H.; Park, Y. H. *Applied and Environmental Microbiology* **2008**, *74*, 2171-2178.

CHAPTER 3

Devulcanization of Scrap Ground Tire Rubber Particles and Successive Carbon Nanotube Growth with Nanostructured Conducting Polymers by Microwave Irradiation

3.1 Introduction

In today's world, very high demands for the production of rubber products,[1] i.e. tires, is the main reason behind the continuous generation of billions of post-consumer scrap tire rubber products,[2] which have emerged as a very serious problem in terms of environmental protection, energy conservation and waste disposal management. More than 170 years,[3] tires have been engineered as the incredible examples of durability with the incorporation of cross-linked sulphur bonds, i.e. C-S and S-S, among highly elastic rubber molecules through a thermodynamically irreversible reaction called "vulcanization" (Figure 27).

When tires have completed their useful lives they can only be accepted by the landfills, for stocking and natural decomposition purposes, after they are ground into small particles. Furthermore, at such landfill areas, scrap tires keep threatening human lives either by causing long term fires, leaking heavy metals into earth while getting naturally decomposed or by hosting disease carrying mosquitoes in their humid and warm environment (Figure 28).[2]

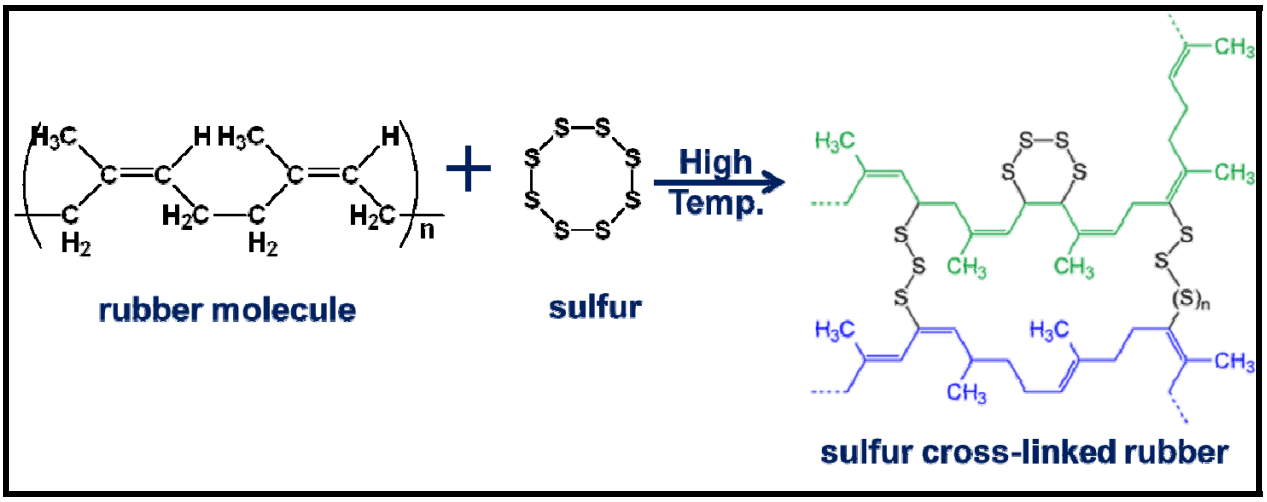

Figure 27. Schematic representation of the vulcanization process

Thus, the majority of the scrap tire problem originates from both the growing sizes of such hazardous landfills and the corresponding increase in the disposal cost of a single scrap tire.[2,4]

Figure 28. Different types of threats caused by the scrap tire landfills; (left) heavy metal leakage into earth during natural decomposition, (middle) ignition of long-term fires along with the emission of hazardous CO and SO_2 gases, (right) hosting disease carrying mosquitoes

Within decades, many researchers from both academia and industry[5] have been targeting their interests and ideas to find the best possible solution for this problem. They come up with strategies which are mainly focused on "recycling and reclamation" in order to utilize the scrap tire rubber crumbs for advanced purposes. The reason is simple that; if those tires can be truly processed, they would provide a huge "virgin rubber" source for the tire manufacturing industry.[4] Likewise, this kind of specially processed tires can be used as fillers or reinforcing agents to improve the various properties of composites built with different polymeric materials, e.g. polyethylene,[6] polystyrene[7-10] and asphalt.[11-14]

Accordingly, many endeavours of researchers have been devoted to generate different kinds of special applications called "devulcanization". As its name implies, this application can be defined as the cleavage of the cross-linked mono, di- and poly-sulfidic bonds among rubber molecules via specific approaches, including mechanic/chemical,[15-17] ultrasonic,[2,4,5] biological[18,19] and microwave[1-3,20,21] treatments (Table 5). The ultimate goal of all these applications, which has only been achieved through microwave and ultrasonic devulcanization methods, is to obtain the maximum amount of devulcanized product that would be identical to the virgin rubber.[21] However, the two common shortages of the ultrasonic method, i.e. (i) targeting incorrect bonds to cleave along the main rubber molecules and causing depolymerisation, thermal destruction or oxidative alterations at primary C-C bonds, and (ii) worsening the physical properties of the resulting devulcanized product,[20] usually limit its applications.

As a result, the microwave devulcanization is worthy to be considered as an option which can properly address the scrap tire problem. In this method, cross-linked sulfidic bonds within ground tire rubber (GTR) particles are severed by the heat of microwave irradiation. The

utilization of microwaves as the heating source provides the great advantage of volumetric heating which ensures faster and more homogeneous devulcanization effect on GTR particles, compared to other heating methods that are based on convection or conduction.[21] Also, the opportunity of treating a large quantity of material in one shot, the continuous characteristic of the process and the tuneable processing parameters,[1] e.g. power level and process time, can be listed as the other major advantages of the microwave devulcanization method.

Table 5. Different types of devulcanization processes

Technology	**Basis of Processing**	**Zone of Reaction**
Chemical	Chemicals/chemical reactions	Surface of particles
Ultrasonic	Ultrasonic waves	Throughout particles
Microwave	Microwaves	Throughout particles
Biological	Microorganisms	Surface of particles
Others	Mechanical, Steam...etc.	Surface of particles

According to the Maxwell-Wagner polarization,[21] materials that would absorb microwaves are required to have a certain polarity. Thus, scrap tire particles, either being inherently polar like polychloroprene, nitrile rubber and chlorinated polyethylene[22] or polarized with the addition of conductive filler[21] "carbon black" are ideal candidates for the microwave devulcanization process. The GTR particles are fraught with difficulties that could negatively affect the resulting quality of the devulcanized GTR (dGTR) particles, which could be majorly

referred as; (i) their thermosetting characteristics caused by the cross-linked sulphur bonds' network and (ii) their compositionally complex nature due to the presence of in-/soluble compounds, such as extender process oil, fillers, additives, curatives and plasticizers.[21] However, microwave devulcanization (i) can provide the optimal conditions and (iii) effectively address all these issues by assuming the recovery of the original chemical formula of elastomers and (iii) their separation from the GTR waste.[20] So, the resulting dGTR product can be (i) used as is, (ii) re-vulcanized into a new rubber product or (iii) blended into a different natural rubber compound without the need of any binding agents.[23] In accordance with all the listed advantages and regarding to both economic and ecological reasons,[20] microwave devulcanization can be considered as one of the best solutions, which can be facilely performed at ambient conditions[24] without the need of any extra chemicals or equipment, for the primarily mentioned scrap GTR problem.[24]

In this study, microwave devulcanization was applied to GTR particles in order to reclaim the maximum amount of raw materials such as virgin rubber and carbon black. And even beyond that, through a previously described PopTube approach,[24] the as-obtained dGTR particles were used as substrates, via the in-situ deposition of nanostructured conducting polymers to grow carbon nanotubes (CNTs) on their surfaces. The resulting particles can be utilized as reinforcing agents for different advanced composite material applications with either conventional polymers,[6-10] CNTs[25,26] or asphalt.[11-14,27]

3.2 Experimental section

3.2.1 Materials and methods

The materials and instruments used in this study include; 40-mesh scrap GTR particles (Blacklidge Emulsions Inc.), pyrrole (Alfa Aesar), hydrochloric acid (HCl, 36-38%, Mallinckrodt Chemical Inc.), ammonium peroxydisulfate (APS, $(NH_4)_2S_2O_8$, 98%, Alfa Aesar), toluene (Alfa Aesar), a standard kitchen microwave (Panasonic Inverter), ferrocene (99%, Alfa Aesar), acetone (VWR BDH) and Lab-line multi unit extraction heater (AB-Line Instruments Inc.).

3.2.2 Devulcanization of scrap GTR particles by microwave irradiation

In a typical experiment, ~5 g of 40-mesh scrap GTR particles were treated in a standard kitchen microwave oven as schematically shown in Figure 29. To ensure better exposure and enhanced devulcanization performance during treatments, GTR particles were spreaded on individual watchglasses.

Since the process variable here was the exposure time,[21] the GTR samples were exposed to fixed microwave power of 1250 W for 1 min., 2 min. and 4 min., respectively. Finally, each sample was identified as “dGTR” followed by a number corresponding to its exposure time in minutes. Upon excessive heat gain, a thick smoke emission was observed especially from the 4 min. treated sample probably due to the evaporation/decomposition of the the process oil compound in it. Here, the process efficiency assessment was made by measuring the amount of virgin rubber-like soluble content collected from each different dGTR sample. Thus, Soxhlet extraction was applied to dGTR samples with toluene as the solvent. After 24 h of extraction, samples in thimble filters and the flasks containing the extracts were dried in an oven at 80 °C for another 24 h, and their mass was measured for comparisons (Table 6).[21]

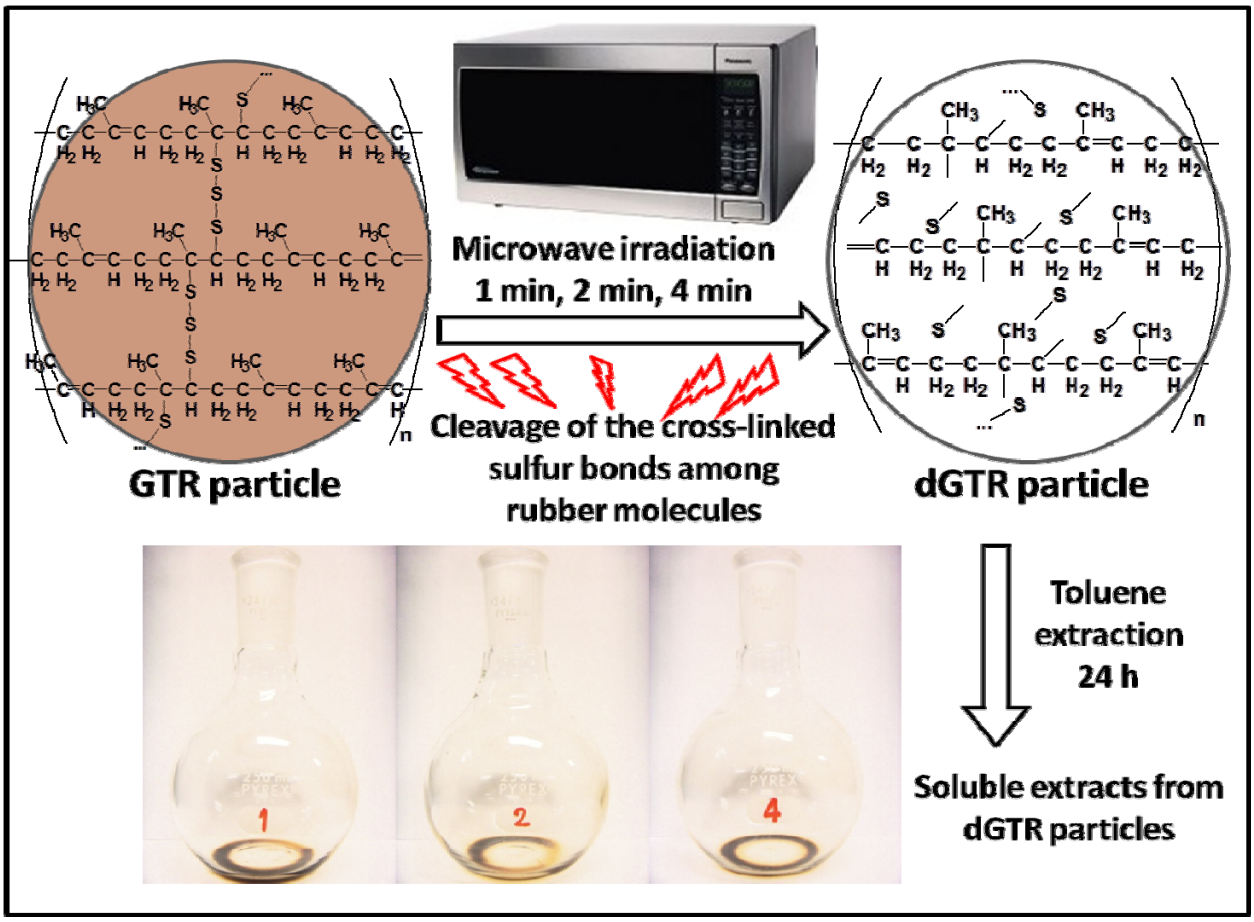

Figure 29. Schematic representation of the microwave-assisted devulcanization of scrap GTR particles and successive toluene extraction process

Table 6. Summary of the weight changes in GTR samples after Soxhlet extraction applied successively to the microwave devulcanization

	Thimble filter 1	**Thimble filter 2**	**Thimble filter 3**
Initial weights	5.4659 g	5.4968 g	5.4637 g
	Thimble filter + Sample 1	**Thimble filter + Sample 2**	**Thimble filter + Sample 3**
Initial weights (before extraction)	9.4618 g	9.4977 g	9.4726 g
	Thimble filter + Sample 1	**Thimble filter + Sample 2**	**Thimble filter + Sample 3**
Secondary weights (after extraction)	8.9440 g	8.9471 g	8.8709 g
	Before/After 1	**Before/After 2**	**Before/After 3**
Weight difference	0.5178 g	0.5506 g	0.6017 g
	Flask 1	**Flask 2**	**Flask 3**
Initial weights (before extraction)	98.2060 g	90.1899 g	84.9388 g
	Flask 1 + Extract	**Flask 2 + Extract**	**Flask 3 + Extract**
Secondary weights (after extraction)	98.7218 g	90.7476 g	85.5386 g
	Before/After 1	**Before/After 2**	**Before/After 3**
Weight difference	0.5158 g	0.5577 g	0.5998 g

3.2.3 Preparation of nanostructured conducting polymer coated dGTR particles

In a typical coating process, 1 g of dGTR particles were added into 50 mL of 1 M aq. HCl medium under magnetic stirring. After 5 min. stirring at ambient conditions, 0.2 mL of pyrrole monomer was added into this mixture. These three compunds were kept stirred for another 5 min., in order to achieve a better homogeneity and exposure in the dispersion. Lastly, 0.23 g of APS salt was added into the reaction medium as the oxidative agent to initiate the polymerization reaction, which lasted for 4 h (Figure 30). At the end of the polymerization/in-situ coating reaction, the dark polypyrrole/dGTR (PPy/dGTR) precipitate was suction filtered while getting washed with copious amounts of 1 M aq. HCl (3 x 100 mL) and acetone (3 x 100 mL). Finally, the as-prepared sample was allowed to dry overnight at ambient conditions.

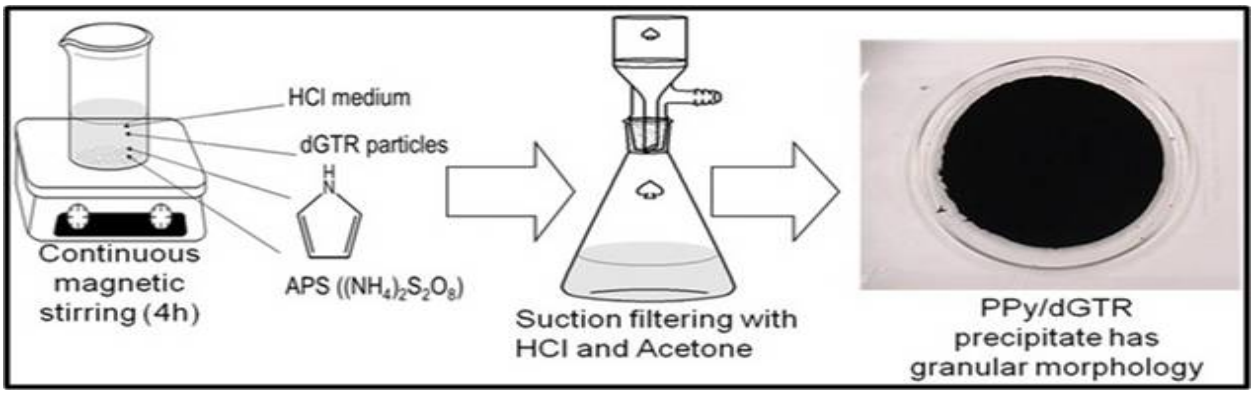

Figure 30. Schematic representation of the in-situ conducting PPy coating of dGTR particles

3.2.4 Carbon nanotube (CNT) growth on PPy/dGTR samples by microwave irradiation

In a standard process, 100 mg of PPy/dGTR sample was mixed with 100 mg of ferrocene precursor, in solid state, at a speed mixer with a rate of 3500 rpm. The as-prepared mixture was transferred in a glass vial, and in the standard kitchen microwave it was continuously exposed to 1250 W microwave irradiation for <1 min. Meanwhile, the ferrocene compound in the mixture

was decomposed to an iron catalyst upon excessive and rapid heat gain through nanostructured PPy coating on dGTR particles' surface as the sample in glass vial started sparking. At this step, the cyclopentadienyl parts of the ferrocene served as the carbon source for the growth of multi-walled (MW) CNTs on dGTR particles' surface. Eventually, the as-produced CNT decorated dGTR particles were collected from glass vials and kept into an oven at 80 °C for the sublimation of any type of organic residues away from the samples, before further characterizations (Figure 31).

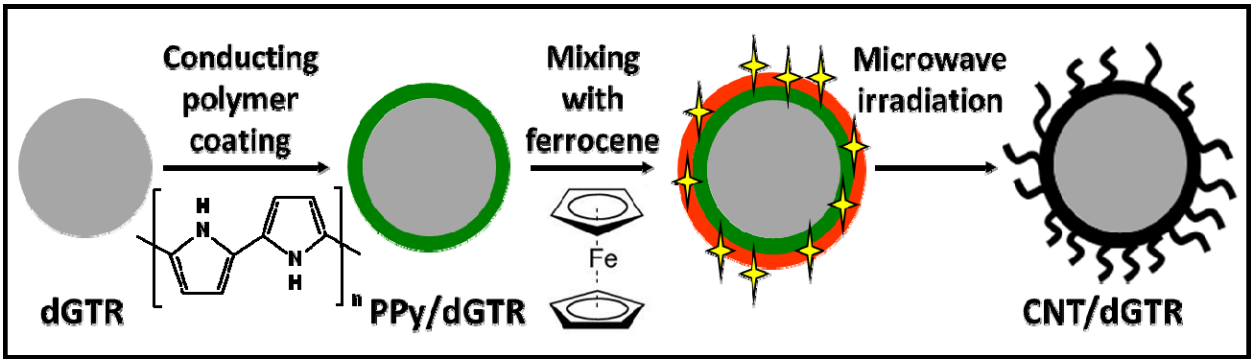

Figure 31. Schematic representation of the microwave-assisted CNT growth process on PPy/dGTR particles

3.2.5 Characterization of the as-obtained samples from different processes

The as-obtained dGTR particles and their extracts were characterized by thermogravimetric analysis (TGA), differential scanning calorimetry (DSC) and Fourier Transform Infrared spectroscopy (FT-IR) in order to verify and prove the success of above-mentioned microwave devulcanization process. Also, morphological features of the nanostructured PPy coated and CNT decorated dGTR samples from the secondary process were characterized by both scanning and transmission electron microscopy techniques.

3.3 Results and discussion

3.3.1 TGA characterization results of the dGTR samples

The TGA characterization was conducted under 50% N_2 / 50% O_2 atmosphere, during which 15 mg of scrap GTR, dGTR1/2/4 and dGTR extract samples were heated from room temperature to 800 °C at a heating rate of 10 °C/min.

Table 7. Summary of the weight changes in different GTR samples during TGA characterization

Sample	Mass loss (%)	Temperature range (°C)
GTR	17.84	200-350
	47.67	350-550
	23.76	550-600
dGTR 1	9.41	200-350
	53.09	350-550
	25.29	550-600
dGTR 2	6.14	200-350
	58.15	350-550
	24.93	550-600
dGTR 4	6.15	200-350
	60.74	350-550
	22.88	550-600
dGTR extract	58.47	200-350
	35.15	350-550

TGA provided very useful information about the thermal properties of different GTR samples, before and after the devulcanization process, such as their overall compositions at a specific temperature range, their decomposition temperatures and their thermo-oxidative behaviors.[21] The summary of the TGA characterization results, i.e. the mass losses ocurred at specific temperature ranges, is shown in Table 7. As it can be seen from this table and Figure 32A, all samples lost the significant amount of their masses at three specific temperature ranges. The initial mass loss ocurred between 200-350 °C was attributed to the decomposition of process oil,[21] which is generally composed of hydrocarbons and is added to the rubber compound to improve its processability. In order to verify this information, the TGA characterization was also applied to the extracted process oil under the same conditions as in GTR samples. Expectedly, the decomposition temperature range of this extract matched with the temperature range of the first inclination point on the GTR samples' thermograms. The secondary mass loss ocurred between 350-550 °C was ascribed to the thermo-oxidation of primary polymeric molecules in GTR samples. Here, longer microwave treatment decreased "the amount of soluble rubber phase" and increased "the relative carbon black content" in dGTR samples due to the effective removal of cross-linked sulfur bonds[21] and degradation of the polymeric rubber molecules. Thus, the thermal stability of the dGTR samples are getting better than the GTR sample, and among them, the longer treated one exhibited a more stable character (Figure 32B). The final mass loss of the samples was ocurred between 550-600 °C due to the thermo-oxidation of the "carbon black" compound,[21] whose proportion in samples was ~24%. Also, most importantly, the amounts of dGTR extracts obtained from the extraction were coinciding with the amounts released from dGTR samples during MW treatments, which were between 13-15% (Table 6).

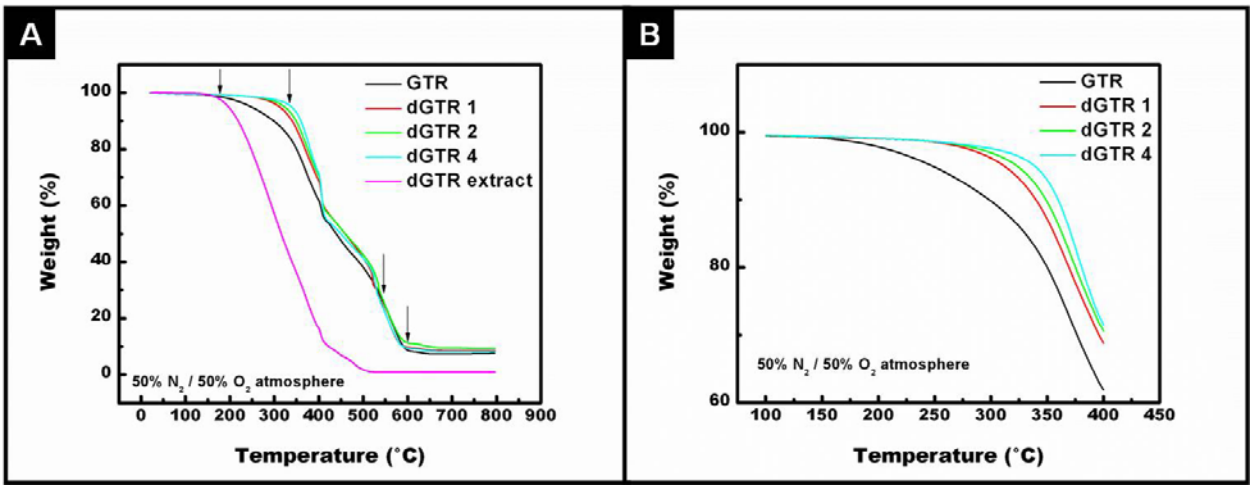

Figure 32. (A) TGA thermograms and (B) Thermal stability comparisons between different GTR samples before and after the microwave devulcanization process

3.3.2 DSC characterization results of the dGTR samples

The DSC characterization was conducted under N_2 atmosphere, during which GTR, dGTR1/2/4 and dGTR extract samples were heated from -100 °C to 400 °C at a heating rate of 10 °C/min (Figure 33). According to the results, the endothermic inflections at low temperatures were ascribed to the glass transition (T_g) temperatures, and the exothermic peaks around 375 °C were ascribed to the decomposition temperatures (T_d) of the samples.[21] There was no significant change observed in the T_g of the GTR, dGTR1 and dGTR2 samples, indicating that the thermal behaviors of these samples at low temperatures were remained similar during microwave treatments. However, the increase in the T_g of dGTR4 reveals the thermal behavior change occurred on this sample during the process, and proves that the effectivity threshold of this application is 4 min.[21] Additionally, upon longer microwave treatment; either (i) the increased carbon black content or (ii) the decreased process oil amount, which works as a plasticizer in GTR samples, can be listed as the other reasons for its increased T_g.[21]

The main purpose of the vulcanization process is to convert the reactive thermoplastic natural rubber molecules into thermoset ones via curing them with sulfur bonds.[1,2,21] Thus, when the reclaimed dGTR extract samples were characterized after microwave devulcanization, they would expectedly exhibit thermoplastic polymer properties. Likewise, this sample exhibited a clear T_g point on its DSC graphic similarly to the dGTR4 sample (Figure 33). As another proof for its thermoplastic property, the wide melting region starting at ~100 °C can be clearly seen from its DSC graphic. Also, the decompositon peak of this sample is located around 375 °C similarly to the previous GTR samples. Through such findings, once more, the success of our microwave devulcanization process has been proven upon the recovery of the virgin rubber component from dGTR particles.

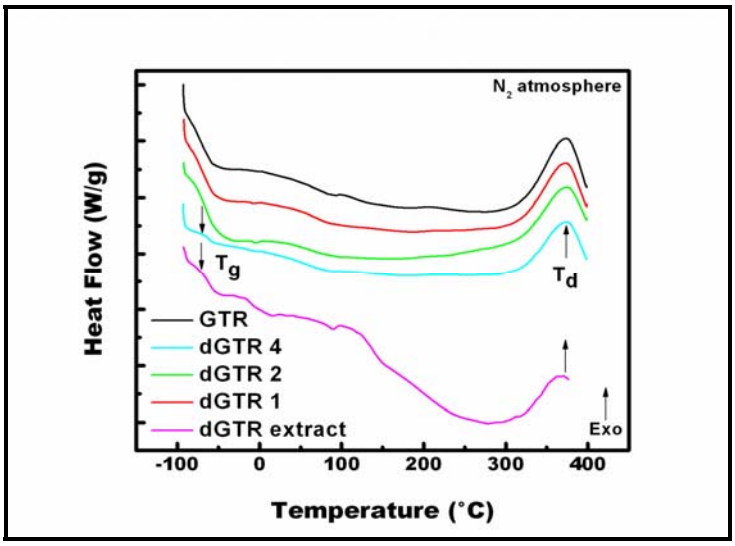

Figure 33. DSC graphics of different GTR samples before and after the microwave devulcanization process

3.3.3 FT-IR spectroscopy characterization results of the dGTR samples

The FT-IR spectroscopy was also applied to GTR and extract samples in order to have a clear idea about the existing functional groups and the possible structural changes that might have occurred on them after the microwave devulcanization process, and collected results are shown in Figure 34A and B.

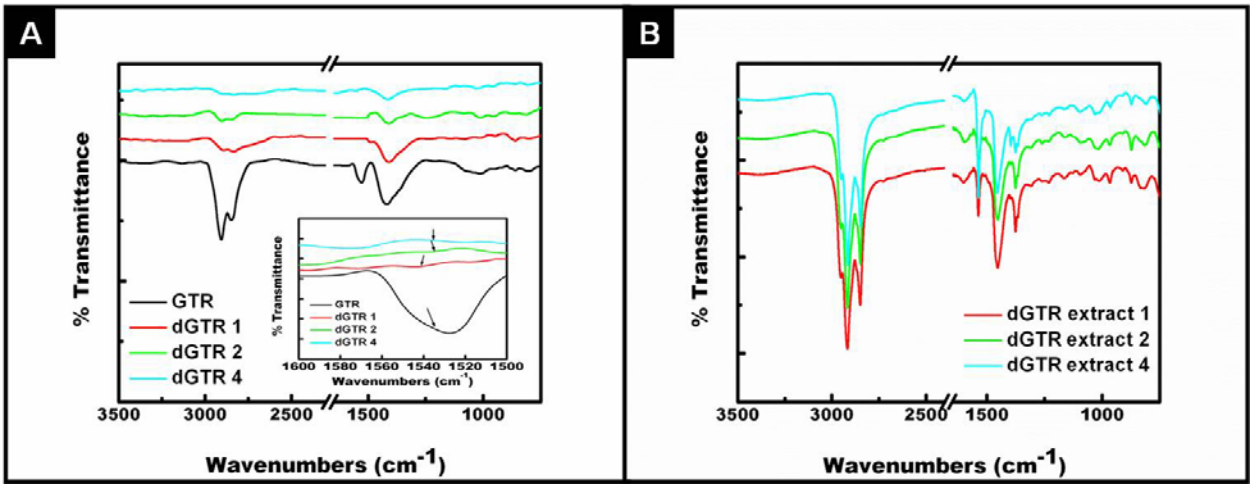

Figure 34. FT-IR spectra of; (A) different GTR samples before and after the microwave devulcanization process (Inset is the FT-IR spectra of the GTR samples showing the intensity changes of the peak around 1540 cm^{-1} upon microwave treatment), (B) different extract samples obtained from dGTR particles

According to the FT-IR spectra of these samples, peaks located between 3000-2800 cm^{-1} correspond to the stretching vibrations of the aliphatic hydrocarbons (C-H) in rubber chains.[16-19,28] The intensity decrease occurred on these peaks after the microwave treatments can be clearly observed in dGTR1/2/4 samples spectra. This was probably due to the scission and disruption of the main polymer chains upon the removal of crosslinked sulfur bonds. The following small peak

around 1600 cm^{-1} corresponds to the axial deformation of a double bond (C=C)[14] which was completely diminished after an effective microwave devulcanization process. The next peak around 1540 cm^{-1} was assigned as the stretching vibration of a methyl assisted conjugated double bond (H_3C-C=CH-).[15-19] The value of this peak was also considerably decreased at the spectra of dGTR1/2 samples and completely disappeared at dGTR4 sample's spectrum due to getting damaged upon longer intensive microwave treatment (Figure 34A inset). This result is also consistent with the efficiency threshold[21] assumption that was made earlier for the 4 min. microwave treatment. The peak located around 1450 cm^{-1} corresponds to the deformation of dihydrocarbons ($-CH_2$),[16-19,28] whose intensity was also decreased after the microwave treatment. Afterwards, the smaller peak around 1375 cm^{-1} corresponds to the methyl group pendanted to the primary rubber chain ($-CH_3$)[14] which was overlapped and disappeared in dGTR samples' spectra.

The following peak around 1020 cm^{-1} indicates the presence of sulfur bonds (C-S)[29] in GTR sample. The diminish in its intensity and disapperance of this peak at dGTR1/2/4 samples spectra proves the effectiveness of the microwave devulcanization applied to these samples. The final peak located around 870 cm^{-1} corresponds to the out-of-plane bending vibration of aliphatic hydrocarbons (=C-H)[28,30] in GTR molecules. The intensity of this peak remained the same at dGTR1 sample's spectrum and significantly decreased at dGTR2/4 samples due to the cleavage of these bonds upon longer microwave treatment.

Eventually, it can be clearly observed from Figure 34B that the dGTR extracts collected from different samples were negligibly different from each other. All of the main functional group peaks appeared on their FT-IR spectra were coinciding, except minimal peak intensity differences, which were probably related with the microwave devulcanization time length of the corresponding dGTR sample, from which the extract was obtained.

After the completion of different characterizations, the resulting dGTR particles were utilized as substrates for a previously described "PopTube" approach.[24] The purpose of this approach is to grow CNTs on dGTR particles' surface within very short time frames via using microwave irradiation at ambient conditions and to produce reinforcing materials for advanced composites built with epoxy, polyethylene[6], polystyrene[7], asphalt[11,14] and so on.

3.3.4 Electron microscopy characterization results of the samples

As shown in Figure 31, (i) dGTR particles were initially coated with PPy during its in-situ polymerization reaction, (ii) PPy coated dGTR particles (PPy/dGTR) were then mixed with ferrocene precursor in solid state and (iii) this mixture was continuously exposed to 1250 W microwave irradiation for <1 min. to generate CNT covered carbonized dGTR particles (CNT/dGTR). The as-obtained samples through this approach were kept into an oven at 80 °C for the sublimation of any type of organic residues away from the samples, and when they were taken out at ambient conditions, further characterizations were conducted with both SEM and TEM, whose results can be seen in Figure 35A-D and Figure 35C inset.

According to Figure 35A, PPy/dGTR sample has a granular-shaped morphology, which is composed of aggregated PPy nanoparticles with average outer diameter sizes ranging between 200-330 nm. This result is consistent with the inherent granular morphologies of both GTR and PPy·Cl.[24] When PPy/dGTR and ferrocene precursor mixture was exposed to microwave energy, they heated up rapidly and started sparking. At this stage, ferrocene was decomposed to an iron catalyst upon excessive heat gain through the PPy coating and the cyclopentadienyl parts in its molecule served as the carbon source for the homogeneously grown MWCNTs[24] covering the dGTR particles' surface (Figure 35B).

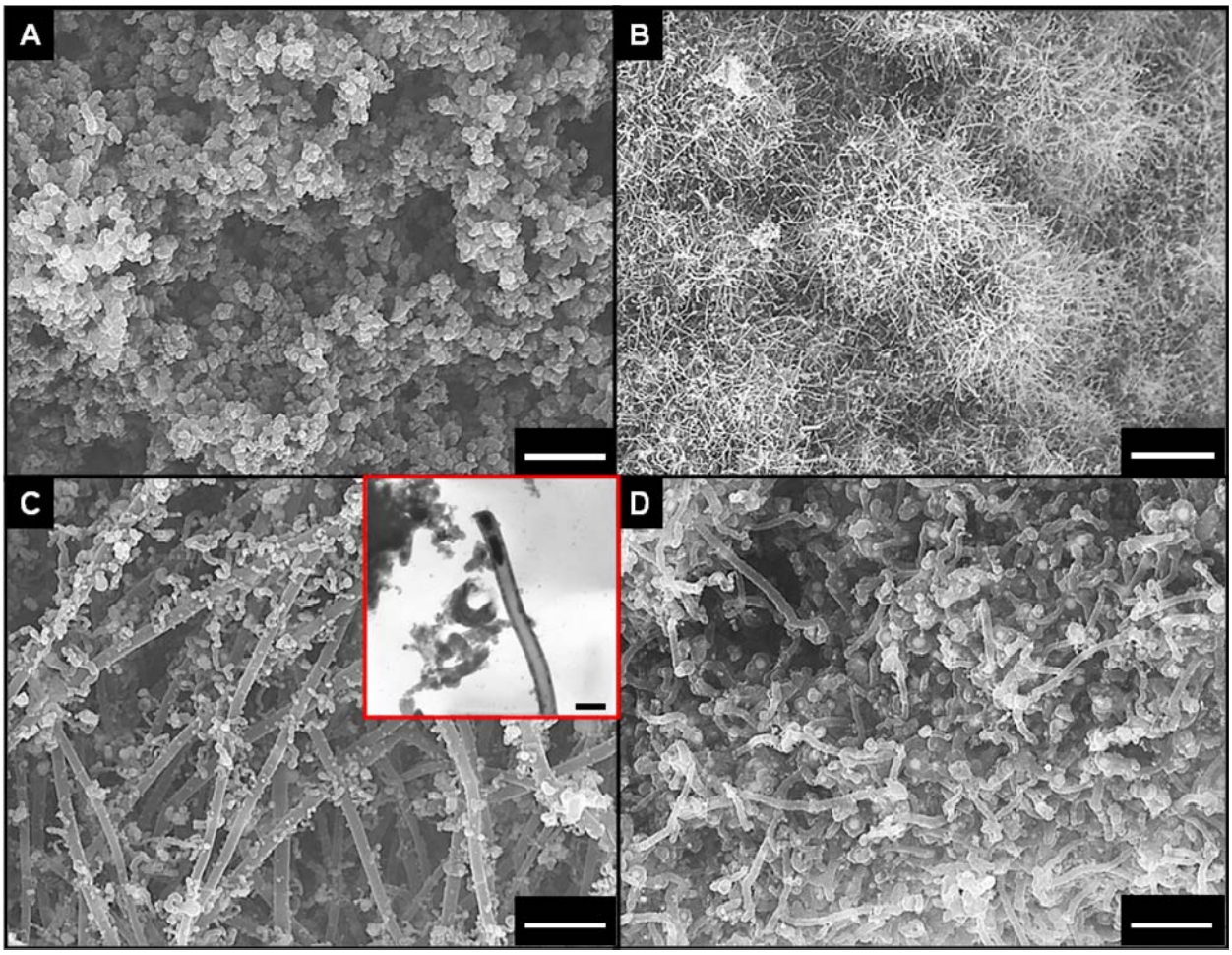

Figure 35. SEM images of; (A) PPy/dGTR sample, (B) CNT/dGTR sample after 1 min. microwave irradiation, (C) Zoomed-in CNT/dGTR sample (Inset is the TEM image of the CNT/dGTR sample showing a hollow CNT with some catalyst iron particles at its tip), (D) Tip-grown CNTs on dGTR particles' surface with iron particles (brighter dots) located at their tips (Scale bars; A: 1 μm, B: 10 μm, C/inset: 1 μm/100 nm, D: 1 μm)

The homogeneity of the CNTs, in terms of growth length and coverage density, can be better understood from Figure 35C, in which, a few micrometers long CNTs with 190-300 nm average outer diameters can be observed along with irregular shaped carbonized GTR residues and also secondarily grown CNTs covering their surfaces. As it was previously proposed for the

PopTube approach, the growth mechanism of these CNTs is also based on the tip-growth model.[24] Due to this reason, most of the iron catalyst particles (brighter dots) were located at the tips of the CNTs and conform the above mentioned growth pattern as it can be seen in Figure 35C inset and 35D.

3.4 Conclusions

The scrap GTR particles have been successfully devulcanized into dGTR products through a short-term microwave irradiation process with an efficiency threshold of 4 min. Furthermore, different characterization results of the as-obtained dGTR particles and the possibility of extracting the virgin rubber component from the devulcanized particles are the other clear indications for the success of this process. Additionally, for the first time, such dGTR particles with nanostructured PPy coating on their surfaces as the microwave energy absorbing/heating layer, were used as substrates to generate a few microns long, tip-grown, hollow CNTs covering their surfaces. We believe the fabrication of this novel material will play an important role for the improvement of "nanostructured engineering material-reinforced polymeric composites".

3.5 References

(1) Zanchet, A.; Carli, L.N.; Giovanela, M.; Crespo, J.S.; Scuracchio, C.H.; Nunes, R.C.R. *Journal of Elastomers and Plastics*, **2009**, *41*, 497-507.

(2) Adhikari, B.; De, D.; Maiti, S. *Progress in Polymer Science*, **2000**, *25*, 909-948.

(3) Fix, S.R. *Elastomerics*, **1980**, *112*, 38-40.

(4) Tukachinsky, A.; Schworm, D.; Isayev, A.I. *Rubber Chemistry and Technology*, **1996**, *69*, 92-103.

(5) Levin, V.Y.; Kim, S.H.; Isayev, A.I.; Massey, J.; vonMeerwall, E. *Rubber Chemistry and Technology*, **1996**, *69*, 104-114.

(6) Sonnier, R.; Leroy, E.; Clerc, L.; Bergeret, A.; Lopez-Cuesta, J.M. *Polymer Testing*, **2007**, *26*, 274-281.

(7) Trifonova, D.; Vasileva, S. *Journal of Materials Science*, **1992**, *27*, 3657-3661.

(8) Crevecoeur, J.J.; Nelissen, L.; Vandersanden, M.C.M.; Lemstra, P.J.; Mencer, H.J.; Hogt, A.H. *Polymer*, **1995**, *36*, 753-757.

(9) Cigna, G.; Matarrese, S.; Biglione, G.F. *Journal of Applied Polymer Science*, **1976**, *20*, 2285-2295.

(10) Alfarraj, A.; Nauman, E.B. *Polymer*, **2004**, *45*, 8435-8442.

(11) Cao, W.D. *Construction and Building Materials*, **2007**, *21*, 1011-1015.

(12) Mull, M.A.; Stuart, K.; Yehia, A. *Journal of Materials Science*, **2002**, *37*, 557-566.

(13) Siddique, R.; Naik, T.R. *Waste Management*, **2004**, *24*, 563-569.

(14) Lima, C.d.S.; Tome, L.G.A.; de Oliveira Filho, C.M.S.; Soares, S.A.; Soares, J.B. *Road Materials and Pavements Design*, **2005**, *X*, 1.

(15) Zhang, X.X.; Lu, C.H.; Liang, M. *Journal of Polymer Research*, **2009**, *16*, 411-419.

(16) Jana, G.K.; Das, C.K. *Macromolecular Research*, **2005**, *13*, 30-38.

(17) Jana, G.K.; Das, C.K. *Polymer-Plastics Technology and Engineering*, **2005**, *44*, 1399-1412.

(18) Li, Y.H.; Zhao, S.H.; Wang, Y.Q. *Polymer Degradation and Stability*, **2011**, *96*, 1662-1668.

(19) Jiang, G.M.; Zhao, S.H.; Luo, J.Y.; Wang, Y.Q.; Yu, W.Y.; Zhang, C.R. *Journal of Applied Polymer Science*, **2010**, *116*, 2768-2774.

(20) Kleps, T.; Piaskiewicz, M.; Parasiewicz, W. *Journal of Thermal Analysis and Calorimetry*, **2000**, *60*, 271-277.

(21) Scuracchio, C.H.; Waki, D.A.; da Silva, M.L.C.P. *Journal of Thermal Analysis and Calorimetry*, **2007**, *87*, 893-897.

(22) Zhang, Z.X.; Chen, C.H.; Gao, X.W.; Kim, J.K.; Xin, Z.X. *Journal of Applied Polymer Science*, **2011**, *120*, 1180-1185.

(23) Li, S.Y.; Lamminmaki, J.; Hanhi, K. *Polymer Engineering and Science*, **2005**, *45*, 1239-1246.

(24) Liu, Z.; Wang, J.L.; Kushvaha, V.; Poyraz, S.; Tippur, H.; Park, S.; Kim, M.; Liu, Y.; Bar, J.; Chen, H.; Zhang, X.Y. *Chemical Communications*, **2011**, *47*, 9912-9914.

(25) Gogotsi, Y. *Science*, **2010**, *330*, 1332-1333.

(26) Xu, M.; Futaba, D.N.; Yamada, T.; Yumura, M.; Hata, K. *Science*, **2010**, *330*, 1364-1368.

(27) Zhu, X.Q.; Lu, C.H.; Liang, M. *Journal of Materials in Civil Engineering*, **2009**, *21*, 699-705.

(28) Arjunan, V.; Subramanian, S.; Mohan, S. *Turkish Journal of Chemistry*, **2003**, *27*, 423-431.

(29) Kannan, G.K.; Gaikewad, L.V.; Nirmala, L.; Kumar, N.S. *Journal of Scientific & Industrial Research*, **2010**, *69*, 841-849.

(30) Fernandez-Berridi, M.J.; Gonzalez, N.; Mugica, A.; Bernicot, C. *Thermochimica Acta*, **2006**, *444*, 65-70.